Chemistry Europe
European Chemical Societies Publishing

WILEY VCH

Excellence in Chemistry Research

Announcing our new flagship journal

- Gold Open Access
- Publishing charges waived
- Preprints welcome
- Edited by active scientists

Meet the Editors of *ChemistryEurope*

Luisa De Cola
Università degli Studi di Milano Statale, Italy

Ive Hermans
University of Wisconsin-Madison, USA

Ken Tanaka
Tokyo Institute of Technology, Japan

ChemSusChem

Research Article
doi.org/10.1002/cssc.202202095

Chemistry Europe
European Chemical Societies Publishing

www.chemsuschem.org

Diffusional Features of a Lithium-Sulfur Battery Exploiting Highly Microporous Activated Carbon

Fernando Luna Lama,[a] Vittorio Marangon,[b, c] Álvaro Caballero,[a] Julián Morales,*[a] and Jusef Hassoun*[b, c, d]

Diffusion processes at the electrode/electrolyte interphase drives the performance of lithium-sulfur batteries, and activated carbon (AC) can remarkably vehicle ions and polysulfide species throughout the two-side liquid/solid region of the interphase. We reveal original findings such as the values of the diffusion coefficient at various states of charge of a Li–S battery using a highly porous AC, its notable dependence on the adopted techniques, and the correlation of the diffusion trend with the reaction mechanism. X-ray photoelectron spectroscopy (XPS) and X-ray energy dispersive spectroscopy (EDS) are used to identify in the carbon derived from bioresidues heteroatoms such as N, S, O and P, which can increase the polarity of the C framework. The transport properties are measured by cyclic voltammetry (CV), electrochemical impedance spectroscopy (EIS), and galvanostatic intermittent titration technique (GITT). The study reveals Li^+-diffusion coefficient (D_{Li}^+) depending on the technique, and values correlated with the cell state of charge. EIS, CV, and GITT yield a D_{Li}^+ within 10^{-7}–10^{-8} $cm^2 s^{-1}$, 10^{-8}–10^{-9} $cm^2 s^{-1}$, and 10^{-6}–10^{-12} $cm^2 s^{-1}$, respectively, dropping down at the fully discharged state and increasing upon charge. GITT allows the evaluation of D_{Li}^+ during the process and evidences the formation of low-conducting media upon discharge. The sulfur composite delivers in a Li-cell a specific capacity ranging from 1300 mAh g^{-1} at 0.1 C to 700 mAh g^{-1} at 2C with a S loading of 2 mg cm^{-2}, and from 1000 to 800 mAh g^{-1} at 0.2C when the S loading is raised to 6 mg cm^{-2}.

Introduction

The mitigation of climate change and global warming recently triggered the limitation of greenhouse gas emission, mainly by developing renewable energy source in alternative to fossil fuels, and electric vehicles (EVs) instead of combustion-engine cars.[1] Meanwhile, the successful management of alternative green energies such as solar and wind, as well as the increase of the EVs driving range and economical sustainability, require adequate energy storage systems.[2] The current lithium-ion batteries (LIBs) based on intercalation or insertion materials both at the cathode and at the anode side have deeply contributed to the development of the modern consumer electronics and boosted the diffusion of the first generation of EVs.[3] In this scenario, many efforts and massive research on alternative batteries characterized by improved energy density, decreased costs and limited flammability have been undertaken to increase the driving ranges, lower the economic impact, enhance the safety content and boost the large-scale diffusion of the EVs.[4,5] Among the various energy storage systems, lithium-sulfur (Li–S) batteries appeared as the most promising candidate due to a two-electron electrochemical reaction providing high theoretical capacity (1675 mAh g_S^{-1}) and energy density (2600 Wh kg^{-1}), with practical values exceeding those of the commercial LIBs.[6,7] In addition, sulfur holds several bonuses, such as great abundance, low-cost and environmental compatibility.[8] Sulfur (S_8) is insulating at the pristine state, with an electronic conductivity of 5×10^{-30} S cm^{-1} at 25 °C, whilst its electrochemical reaction in lithium cell involves the formation of both insoluble species such as Li_2S_2 and Li_2S that may precipitate in the cell environment, and soluble high-order lithium polysulfides (Li_2S_x, $4 \leq x \leq 8$).[9] The above mentioned low conductivity may actually hinder the Li-ion mobility and diffusion, thus lowering the active material utilization and increasing the cell polarization.[9] The ions diffusivity in a poorly conductive environment such as the Li–S system has actually a crucial role in driving the cell performances, particularly in terms of overall impedance and rate capability. This aspect has been in part highlighted in various literature reports,[10,11] however, its full understanding still needs specific efforts and researches. Moreover, the electrochemically active soluble lithium polysulfide intermediates can be directly reduced at the

[a] F. L. Lama, Prof. Dr. Á. Caballero, Prof. Dr. J. Morales
Department of Química Inorgánica e Ingeniería Química
Instituto de Química Fina y Nanoquímica
University of Córdoba
14071 Córdoba (Spain)
E-mail: iq1mopaj@uco.es
[b] Dr. V. Marangon, Prof. Dr. J. Hassoun
Department of Chemical, Pharmaceutical and Agricultural Sciences
University of Ferrara
Via Fossato di Mortara 17, Ferrara 44121 (Italy)
E-mail: jusef.hassoun@unife.it
[c] Dr. V. Marangon, Prof. Dr. J. Hassoun
Graphene Labs, Istituto Italiano di Tecnologia
Via Morego 30, 16163 Genova (Italy)
E-mail: jusef.hassoun@iit.it
[d] Prof. Dr. J. Hassoun
National Interuniversity Consortium of Materials Science and Technology (INSTM)
University of Ferrara
Via Fossato di Mortara 17, 44121, Ferrara (Italy)

Supporting information for this article is available on the WWW under https://doi.org/10.1002/cssc.202202095

lithium surface to form an irregular solid electrolyte interphase (SEI) layer which increases the cell impedance and gradually decreases the capacity.[12] The soluble fraction of the latter reduced species can migrate by diffusion from the anode back to the cathode to be newly oxidized and undergo a loop reaction indicated as shuttle process leading to a continuous charge without any energy storage, loss of active material, fast capacity fading and poor Coulombic efficiency.[13–15] Therefore, the proper design of suitable electrolyte media was deeply investigated for allowing sufficient safety in view of the use of lithium metal anode, high ionic conductivity and transport number, as well as an adequate SEI at the electrodes, particularly at the Li surface. The most employed electrolyte for Li–S cell consisted of a solution of a lithium salt (e.g., lithium bis(trifluoromethanesulfonyl)imide (LiTFSI)) in dioxolane (DOL) and dimethoxy ethane (DME), which was successfully upgraded by the addition of lithium nitrate as sacrificial specie which can form a SEI at the lithium surface including carbonates and nitrates strongly limiting the polysulfide shuttle process.[16] The replacement of DOL and DME with lowly flammable solvents such as glymes (i.e., ethers with formula $CH_3O(CH_2CH_2O)_nCH_3$ and $n \geq 2$)[17] or polymers (e.g., solid polyethylene glycol dimethyl ether, PEGDEM)[18] has been indicated as the most suitable pathway to improve the cell safety. The most explored strategy to mitigate the issues affecting the Li–S cell is to accommodate the sulfur in conductive carbon matrixes, such as graphene and its derivatives,[19] carbon nanotubes,[20] carbon nanofibers,[21] hollow carbon spheres[22] or porous carbons.[23] Indeed, suitable carbon additives can actually enhance the reaction kinetics and the cell performance by ensuring high electronic and ionic conductivity, large surface area and well-ordered pore systems which hold the contact with sulfur and lithium polysulfides by physical absorption via weak van der Waals interaction, and accelerate the electron/ion transfer.[24–26] Furthermore, the inclusion into the above mentioned carbon hosts of nanometric metals,[10,11] metal oxides,[27] conductive polymers,[28] MOFs,[29] or doping heteroatoms[30] can lead to additional polysulfide anchoring by chemical absorption. The synergistic combination of both physical and chemical adsorption sites in the conductive matrix limits excessive polysulfide shuttle and enhance the active sulfur utilization, thus providing improved cycling stability and a high-energy density,[31,32] and possibly allowing simple synthetic pathways for potential scaling-up.[33,34] Recently, the use of biomass wastes to prepare carbonaceous materials for energy storage systems has been considerably increasing due to their abundance, accessibility, low-cost and sustainability.[35] A wide range of biomass-derived carbons from different sources, such as olive stone,[36] cherry pits,[37] banana peels,[38] brewing wastes,[39] goat hair,[40] silk cocoon,[41] luffa sponge[42] and tobacco stems[43] among others, have been employed as stable sulfur hosts with high surface area and tuned pore size in efficient lithium batteries, including the Li–S one. A common route for improving the electrochemical response of these carbons involves activation process with the aim of modifying the porous texture and increasing their absorption properties. Chemical activations with KOH or H_3PO_4 are among the most diffused pathways, where the latter allows the formation of larger pores suitable for sulfur and polysulfides hosting.[44] Indeed, pore shape and distribution into the carbon structure can play a key role in enhancing the Li–S electrochemical process. For instance, micropores (<2 nm) are capable to anchor the soluble intermediate polysulfides by strong interactions, thus improving the cycling stability. Instead, mesopores (2–50 nm) and macropores (>50 nm) may enable fast Li^+/e^- transport, shorten the diffusion pathways, and enhance the rate capability.[45] Furthermore, doping with heteroatoms such as N, O, S or P can alter the carbon framework polarity and facilitate the chemical adsorptions, thus alleviating the shuttle effect and improving the sulfur utilization.[46,47] We previously reported various activated carbons derived from biomass of different nature for Li–S batteries with promising results.[37,48–50] Herein, we use a mango pit-derived activated carbon (MPAC), which was recently exploited to achieve high performing sulfur composites for Li cells.[51] Mango is one of the most widespread fruits with a production of more than 54 million metric tons in 2020[52] and its processing into finished products generates a substantial amount of waste dominated by lignocellulosic pit. These wastes can be converted into activated carbon with H_3PO_4,[51] which is used in this work to achieve a composite with S content increased both in the composite up to 90% and in the electrode up to 6 mg cm^{-2}, possibly benefitting from the presence of heteroatoms as synthesis residuals. Most importantly, we focus the attention on the ion diffusion characteristics of the electrodes in Li–S cells by means of different electrochemical methods to fully understand the characteristics of this complex energy storage system, and shed light on efficient strategies to actually trigger the best performances and allow the scaling-up of cells of practical interest in terms of energy density and cycle life.

Results and Discussion

A preliminary physical-chemical investigation of the MPAC used for the preparation of the sulfur composite is reported in Figure 1. The XRD pattern in Figure 1a exhibits a relevant background and two broad peaks around 23° and 44° in 2θ range suggesting a very limited graphitic character. Indeed, the first peak, which is possibly indexed to the (002) plane of the natural graphite, has a relevant width, a low intensity and a relatively high d spacing, while the second one is even less defined and may be hardly ascribed to the planes (100) and (101).[53] These features are typical of highly disordered carbons with structural hallmark of the activated carbons derived from biomass.[54] The Raman spectrum of Figure 1b agrees with the latter description since it exhibits two peaks around 1333 and 1603 cm^{-1} assigned to I_D (forbidden in graphite) and I_G, respectively, with relatively high value of the I_D/I_G ratio (i.e., 0.87), thus suggesting a high disorder degree likely promoted by the adopted synthesis conditions.[55,56] The thermogravimetric analysis (TGA) curve of the MPAC recorded under O_2 atmosphere (Figure 1c) shows an initial weight loss due to absorbed H_2O (2.8%), a continuous weight loss between 450–750 °C (94.5%) predominantly due to the combustion of the

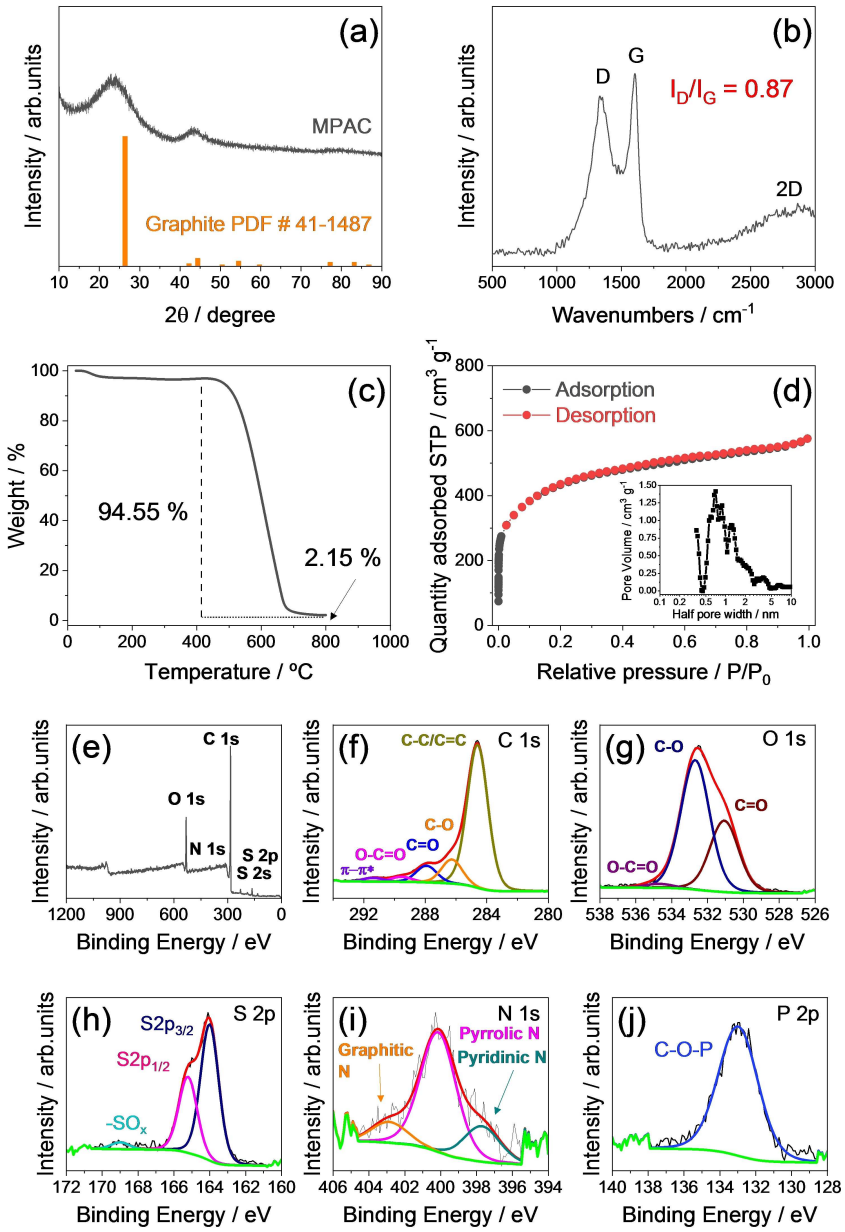

Figure 1. Physical–chemical characterization of the MPAC sample. In detail: (a) X-ray diffractogram, where reference data for graphite (orange bars, PDF #41-1487) are reported for comparison; (b) Raman spectrum, with intensity ratio of the D and G peaks reported in inset; (c) TGA performed in the 25–800 °C temperature range under O_2 flow; (d) N_2 adsorption-desorption isotherm, inset displays the pore size distribution obtained through DFT method; (e–j) XPS analyses, in particular, (e) survey spectrum (see Figure S1 in the Supporting Information for a magnification of the low binding energy region) and (f) C1s, (g) O1s, (h) S2p, (i) N1s, and (j) P2p regions related spectra (the fitted line is highlighted in red color to distinguish from black experimental line). See the Experimental Section for acronyms.

carbon matrix and possibly organic residuals, and a final ash content of 2%. Furthermore, the N_2 adsorption/desorption isotherms of MPAC (Figure 1d) reveal the characteristic shape of a microporous solids belonging to the type I in the BDDT classification, while the almost absence of hysteresis between the two curves suggests the scarcity of mesopores as indeed confirmed by the distribution curve in inset with a pore size ranging between 0.3 and 3.0 nm.[55,56] The data of Figure 1d allow the determination of a specific surface area (S_{BET}) of 1559 $m^2 g^{-1}$, a micropore area ($S_{micropore}$) of 1019 $m^2 g^{-1}$, and a total pore volume ($V_{micropore}$) of 0.73 $cm^3 g^{-1}$, i.e., values expected to allow a high S content in the composite.[50] Additional characteristics of the activated carbon are given by the XPS survey spectrum in Figure 1e, which clearly shows the presence of peaks assigned to C, O, N, S and P with atomic percentage reported in Table 1, as well as a very weak signal assigned to Cl (see magnification of the low binding energy region in Figure S1 of the Supporting Information). The C1s photoemission peak (Figure 1f) is fitted to six components attributed to the C–C bond, the C–O bonds of the hydroxy, carbonyl, and

Table 1. Element percent concentrations detected in the MPAC sample by XPS and EDS. See Figure 1 and Figure S3 in Supporting Information, respectively, for the corresponding analyses, and Experimental Section for acronyms.

Element	C	O	S	N	P	Cl
XPS [at%]	82.60	12.79	1.95	1.61	0.91	0.14
EDS [wt%]	84.60	8.40	4.90	Not detected	1.80	0.30

carboxyl groups, and the π-π* transition (wake-up).[57] It is worth mentioning that the above fit neglects the interactions of C with N and S, since their energy differs is very close to that of the C–O bond, although some literature possibly includes them within the C1s signal fitting.[58,59] The O1s peak (Figure 1g) is fitted according to three components associated with the C functional groups discussed above.[60] Therefore, in line with the fit of the C1s peak, the most intense O1s component corresponds to the C–O functional group, while the less intense one to the O–C=O group.[61] On the other hand, the S2p peak (Figure 1h) reveals an intense signal ranging from 162 eV to 165 eV with a characteristic doublet assigned to the C–S bond, and a weak shoulder between 167 eV and 170 eV attributed to the S–O bond.[61] The N1s peak (Figure 1i) fits to three components assigned to pyridinic N (397.7 eV), pyrrolic N (400.1 eV) and graphitic N (402.9 eV),[62] while the symmetrical P2p peak centered at 133.0 eV (Figure 1j) can be fitted with a single component assigned to P–O[63] or C–O–P bonds.[64] A morphological insight on the MPAC is given by the SEM images in Figure S2 (Supporting Information) which exhibit agglomerated microparticles leading to interconnected pores, as typically observed in different activated carbons.[63–66] In addition, the EDS analysis performed on the SEM image (Figure S3) reveals, beside the carbon, the presence of O, P, S and Cl elements with amounts slightly differing from those revealed by XPS (see Table 1), while N is not detected. These apparent discrepancies are likely ascribed to the different principles on which the two techniques are based. Light elements are difficult to identify in EDS because of the low energy Kα radiation (less than 1 keV). On the other hand, N appears as a trace element in the sample, unlike C and O which are the predominant elements and share similar X-ray energies (227, 392 and 525 eV for C, N and O, respectively).

The lithium polysulfides retention ability of the MPAC is tested through UV/Vis and XPS measurements carried out on a Li_2S_6 solution (see preparation in Experimental Section) at the pristine state and upon aging in contact with the activated carbon, as reported in Figure 2. Photographic images reveal a notable change of color of the MPAC-treated solution upon 6 h of aging (compare Figure 2a and b) that modifies from yellow to a transparent shade indicating the absorption of the lithium polysulfides, while the pristine solution maintains its original color.[67] The polysulfides entrapment is confirmed by the UV/Vis measurements performed on the Li_2S_6-containing solutions (Figure 2c) that show the vanishing of the peak ascribed to lithium polysulfides at 460 nm upon aging in contact with the MPAC.[68] XPS data obtained from the pristine Li_2S_6 solution and the MPAC sample aged in contact with Li_2S_6 for 6 h (MPAC@Li_2S_6) provide additional insight on the interaction

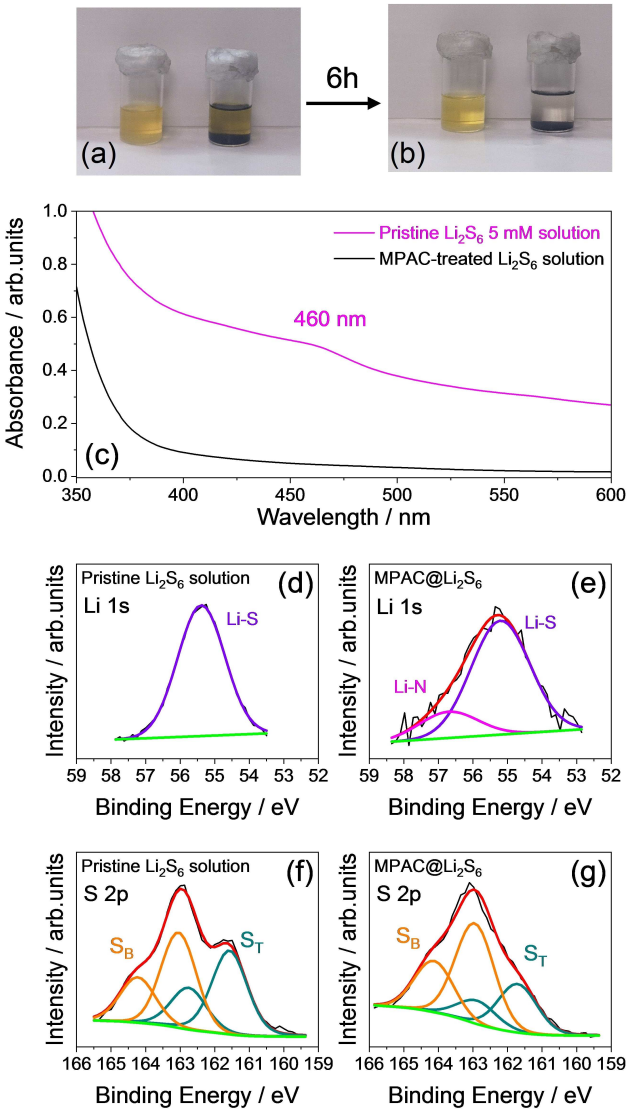

Figure 2. Evaluation of lithium polysulfides retention ability of the MPAC sample. In detail: (a, b) photographic images (a) at the initial stage and (b) after 6 h aging of the pristine Li_2S_6 solution (left-hand side) and the MPAC-treated Li_2S_6 solution (right-hand side); (c) UV/Vis measurements of the Li_2S_6 solution and of the one aged in contact with MPAC for 6 h; (d–g) XPS spectra related to (d, f) the pristine Li_2S_6 solution and (e, g) the MPAC sample aged in contact with Li_2S_6 for 6 h (MPAC@Li_2S_6) in the (d, e) Li1s and (f, g) S2p regions (the fitted line is highlighted in red color to distinguish from black experimental line). See Experimental Section for acronyms.

between carbon and polysulfides (Figure 2d–g). The Li_2S_6 solution at the pristine state exhibits in the Li1s region a single signal centered around 55.4 eV ascribed to the Li–S bond (Figure 2d), while a second additional peak can be identified at about 56.6 eV for the MPAC@Li_2S_6 (Figure 2e) due to the

interaction between Li and the N traces in the MPAC.[69] Moreover, the S2p spectrum of the pristine Li_2S_6 solution (Figure 2f) exhibits two double-signals at 161.6 ($S2p_{3/2}$)/162.8 eV ($S2p_{1/2}$) and 163.1 ($S2p_{3/2}$)/164.3 eV ($S2p_{1/2}$), respectively assigned to terminal sulfur (S_T) and bridging sulfur (S_B) which experience significant changes in the corresponding spectra of the MPAC@Li_2S_6 (Figure 2g).[68,70] Indeed, both the S_T and S_B signals shift to higher binding energies, that is, 162.9 ($S2p_{3/2}$)/163.9 eV ($S2p_{1/2}$) and 164.0 ($S2p_{3/2}$)/165.0 eV ($S2p_{1/2}$), respectively, thus suggesting a decreased electron density of the sulfur atoms due to C–S interaction mainly through S_T groups.[68,69,71] The remarkable interaction of S_T with the MPAC is also evidenced by the decreased intensity of the respective signals, despite further changes of the peaks due to the presence of S traces in the MPAC cannot be excluded.

The MPAC is hereafter employed for the preparation of the sulfur composites according to the sketch in Figure S4 (Supporting Information), which includes also the activated carbon synthesis beginning from the mango pits. It is worth mentioning that the carbonization step of the precursor to achieve the MPAC (see Experimental Section and left-hand side of Figure S4, Supporting Information) removes by pyrolytic decomposition the non-carbonaceous elements which are converted to volatile compounds to form multiple structural defects, thus strongly affecting the environment of the carbon atoms and giving rise to wrinkled sheets packed with a high degree of disorder as previously discussed in Figure 1. Moreover, the H_3PO_4 acid promotes bond cleavage through surface oxidation to form phosphate and polyphosphates bridges that connect and crosslink the biopolymer fragments.[72] Indeed, the complete dehydration of phosphoric acid at elevated temperatures can lead to P_4O_{10} which may attack the carbon surface, thus leading to the development of the above discussed complex micropore system with high surface area (see Figure 1d). On the other hand, the subsequent moderate-temperature melting-assisted sulfur incorporation into the MPAC to achieve the S@MPAC samples (see Experimental Section and right-hand side of Figure S4, Supporting Information) actually represents a facile pathway suitable for avoiding side reactions that can affect the reactivity in lithium cell and, at the same time, finely tuning the sample composition, and triggering possible scalability of the electrode material.[26,34] Therefore, the synthesis allows the preparation of the three electrode materials S@MPAC-73, S@MPAC-82, and S@MPAC-91, with sulfur content increasing from 70 to 80 and to 90 wt%, respectively, which are characterized in terms of structure, morphology, and composition by combining various investigation techniques in Figure 3. The XRD patterns in Figure 3a clearly exhibit the diffraction peaks of the orthorhombic S (S_8, PDF #08-0247), i.e., the most stable crystalline phase to which the molten sulfur tends to solidify back, rather than the amorphous one observed in other synthetic pathways.[73–75] Furthermore, the C component is identified by the broad peak located between 15° and 35° in 2θ range, with a decreasing intensity as the S content increases. It is worth mentioning that the absence of side peaks typical of degraded sulfur samples further suggests the mild-conditions used herein as suitable for scaling up. The sulfur content in the composites is evaluated by thermogravimetry under N_2 atmosphere, and the corresponding weight losses together with that of bare S are plotted in Figure 3b. The figure likely indicates the correspondence between the initially projected S to C mass ratios (i.e., 70:30, 80:20 and 90:10) and the ones achieved for the composites after synthesis, thus indicating the almost complete absence of sulfur evaporation during the process.[76] The TGA profiles of Figure 3b, and the corresponding differential curves (DTG) reported in Figure S5 (Supporting Information) reveal significant differences. Hence, S evaporates from the composites within temperature ranging from 200 to 450 °C, instead the pure S shows an interval restricted between 200 and 330 °C. In addition, pure S shows a single TG slope (Figure 3b), represented by one peak in the corresponding DTG (Figure S5), while the composites reveal two TG slopes, with a peak and an additional high-temperature shoulder in the DTG curve having an intensity decreasing by S content increase. This trend suggests the presence of sulfur particle differently interacting with the carbon host in the composites, that is: i) a more volatile sulfur fraction mainly located in external shells weakly linked to carbon and represented by the peak at lower temperature in the DTG (Figure S5); ii) a less volatile sulfur fraction located near by the surface or within the micropores of the host in internal shells, represented by the shoulder at higher temperature in the DTG, which is more relevant at increasing carbon contents.[77,78] The morphology of the S@MPAC composites is subsequently investigated by SEM at various magnifications (Figure 3c–h). The micrographs show for all samples aggregates of sulfur and carbon with a size of about 50 μm, and an apparent porosity decreasing by increasing the sulfur content from S@MPAC-73 (Figure 3c, d) to S@MPAC-82 (Figure 3e, f) and to S@MPAC-91 (Figure 3g, h).

The EDS mapping included in Figure S6 (Supporting Information) shows a very homogeneous distribution of the sulfur into the carbon matrix, with magnitude increasing by raising the sulfur content in the S@MPAC composite from 70 wt% to 80 wt% and to 90 wt%. The optimal structure and morphology observed in Figure 3 are expected to boost an efficient diffusion of the ions within the electrode matrix for allowing optimal operation of the Li–S cell. Furthermore, the chemical nature of the S@MPAC electrodes is investigated by XPS and the outcomes are reported in Figure 4. The survey spectra of S@MPAC-73 (Figure 4a), S@MPAC-82 (Figure 4d) and S@MPAC-91 (Figure 4g) clearly show the signals of C, O, and S. Instead, the N, P and Cl traces previously detected in the MPAC (see Figure 1 and Table 1) are no longer observed due to their marginal contribution which is further lowered by the predominant presence of sulfur in the composites with respect to the carbon. The XPS C1s peaks (Figure 4b, e and h, respectively) can be likely fitted to the same components used for the MPAC host (compare with Figure 1f). The figure also evidences the intensity increase of the component assigned to the C–O bond compared to that of the C=O bond as the S content in the composite raises, particularly for S@MPAC-91 (Figure 4h), as most likely ascribed to the relevant contribution of the C–S bond. Analogously to the C1s signal, also the S2p peak in Figure 4(c, f, and i) shows a very a similar shape compared to

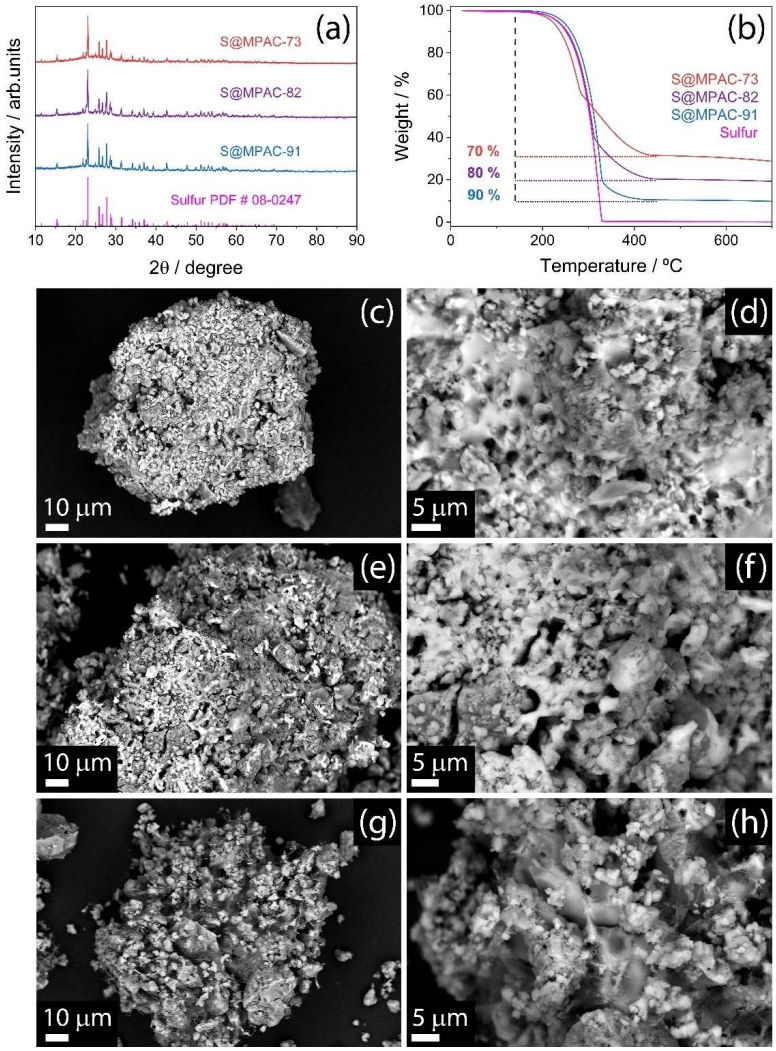

Figure 3. Physical–chemical study of the S@MPAC composites. In detail: (a) X-ray diffractograms, reference data for sulfur (magenta bars, PDF #08-0247) are reported for comparison; (b) TGA of the S@MPAC composites and elemental sulfur powder carried out under N_2 flow between 25 and 700 °C (see Figure S5 in the Supporting Information for corresponding DTG); (c–h) SEM images at various magnifications of (c, d) S@MPAC-73, (e, f) S@MPAC-82 and (g, h) S@MPAC-91. See Experimental Section for acronyms.

the corresponding peak in the MPAC (compare with Figure 1h). However, the intense doublet can be attributed in the composites to S–S bonds rather than C–S of the MPAC, since C–S and S–S binding energies are very similar,[61] while only traces of SO_x species can be detected. The chemical features of the composites detected in Figure 4 suggest once more the absence of side compounds that may possibly affect the Li–S cell response, cause uncontrolled increase of the overall resistance, slow down the kinetics, and negatively influence the electrode/electrolyte interphase stability, thus leading to system failures in particular upon prolonged discharge/charge cycling.

The electrochemical features of the S@MPAC composites in Li–S cells are investigated by coupling cyclic voltammetry (CV) and electrochemical impedance spectroscopy (EIS), with the results reported in Figure 5. During the first cycle, the voltammetry curves (Figure 5a, c and e) reveal the profile expected by the conversion reaction between Li and S, with cathodic scan resolved in two well-defined reduction peaks around 2.3 and 1.9 V vs. Li^+/Li associated with the formation of high-order (Li_2S_x, $4 \leq x \leq 8$) and low-order (Li_2S_x, $2 \leq x \leq 4$) lithium polysulfides, whilst the subsequent anodic scans show the oxidation back to lithium and sulfur according to a double overlapped wave with potential ranging from 2.1 to 2.5 V vs. Li^+/Li.[79,80] Relevantly, the three electrodes show differences in the curves shape, with a signal magnitude and definition increasing and peak width decreasing by raising the S content. Indeed, S@MPAC-73 evidences the broadest peaks (Figure 5a), S@MPAC-91 shows the narrowest ones (Figure 5e), while S@MPAC-82 reveals an intermediate shape (Figure 5c), thus accounting for kinetics changes promoted by sulfur-to-carbon ratio increase. All the materials are characterized by a decrease of cell polarization upon the first cycle, with reduction peaks shifting to higher potentials and oxidation peaks to lower values, and by subsequent, almost overlapped profiles with

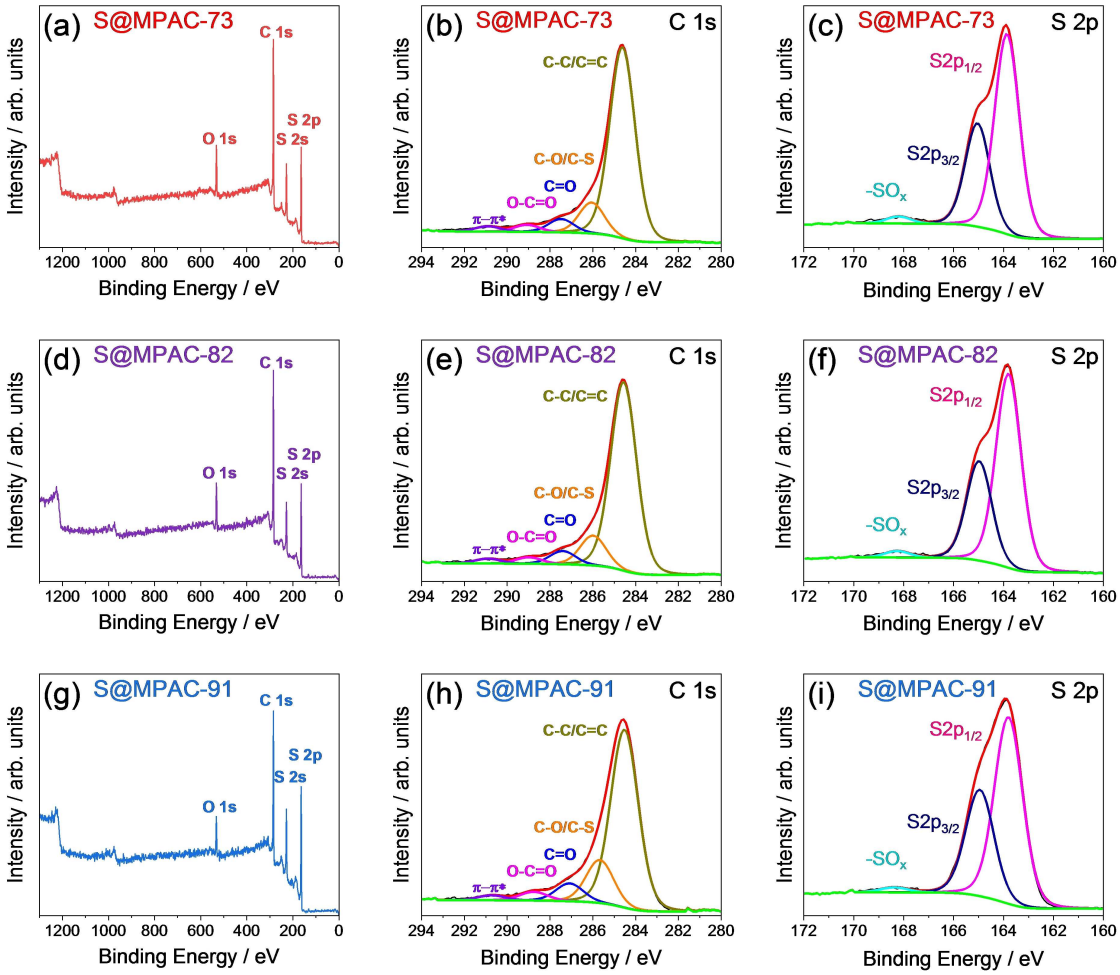

Figure 4. XPS investigation carried out on the (a–c) S@MPAC-73, (d–f) S@MPAC-82, (g–i) S@MPAC-91 composites. In particular: (a, d, g) survey, (b, e, h) C1s and (c, f, i) S2p spectra (the fitted line is highlighted in red color to distinguish from black experimental line). See Experimental Section for acronyms.

minor intensity decrease due to a limited active material loss possibly occurring during the CV tests.[10] The above mentioned cell polarization decrease, which is typically indicated as electrochemical activation process, can be ascribed to a favorable electrode structural and morphological modifications, promoted by lithium polysulfide dissolution during discharge and subsequent sulfur deposition during charge, occurring at the first cycle.[10,11,81,82] This intriguing improvement is well justified by the EIS measurements carried out at the OCV condition of the cell and upon CV, and analyzed by non-linear least square (NLLS) method according to an equivalent circuit composed of resistive (R) and constant phase elements (CPE, Q), identified by the $R_e(R_iQ_i)Q_w$ model. The R_e is the electrolyte resistance determined by the high-frequency intercept in the Nyquist plots, R_i and Q_i elements (R_iQ_i) identify high-to-medium-frequency semicircles related to the electrode/electrolyte interphase (the number of which depends on the material and the considered CV cycle), while R_w and Q_w indicate the Warburg-type Li^+ diffusion represented either by a low-frequency semicircle (R_wQ_w) or by a tilted line (Q_w) in the same frequency region.[83,84] Indeed, the results of the NLLS analysis reported in Table 2 evidence the decrease of the overall interphase resistance (R_{total}) from about 25, 27, and 30 Ω at the OCV to about 7, 2, and 3 Ω after one cycle of the cells using S@MPAC-73 (Figure 5b), S@MPAC-82 (Figure 5d), and S@MPAC-91 (Figure 5f), respectively. The relevant decrease of the interphase resistance is in line with the improvement of the CV profile, while the subsequent stabilization to low and stable values well supports the overlapping of the subsequent voltammetry cycles.

The diffusional characteristics study of the lithium ions into the S@MPAC electrode/electrolyte interphase represent a key aspect for fully understanding the Li–S cell features. The Li^+ diffusion coefficient ($D_{Li}{}^+$) can be evaluated using several electrochemical techniques, including CV, EIS and GITT as reported in Figure 6. Indeed, the CV curves collected at various scan rates (Figure 6a-c) allows the determination of $D_{Li}{}^+$ from the relationship between the peak current intensity (I_{peak}, [A]) and the square root of the scan rate according to the Randles-Sevcik Equation (1):[81]

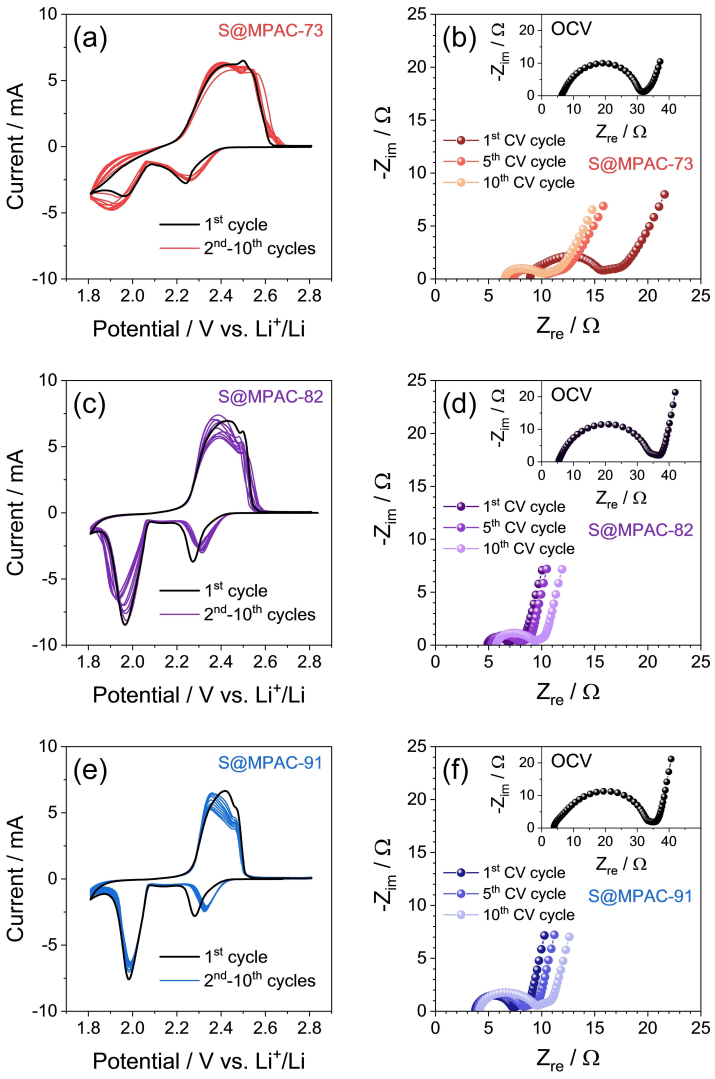

Figure 5. (a, c, e) CV and (b, d, f) EIS measurements performed on Li | DOL : DME, 1 mol kg^{-1} LiTFSI, 1 mol kg^{-1} $LiNO_3$ | cathode cells employing either (a, b) S@MPAC-73, (c, d) S@MPAC-82 or (e, f) S@MPAC-91. CV carried out at the scan rate of 0.1 mV s^{-1} between 1.8 and 2.8 V vs. Li^+/Li; EIS performed in the 500 kHz to 0.1 Hz frequency range by applying an alternate voltage signal of 10 mV at the OCV cell condition (see related insets) and upon, 1, 5 and 10 CV cycles. See Experimental Section for acronyms.

Table 2. NLLS analyses of the Nyquist plots reported in Figure 5 recorded by EIS upon CV performed on Li | DOL : DME, 1 mol kg^{-1} LiTFSI, 1 mol kg^{-1} $LiNO_3$ | S@MPAC cells. Equivalent circuits and resistance values were obtained with the aid of the Boukamp software.[83,84] R_1 and R_2 represent the interphase resistance values in the (R_iQ_i) elements and their sum identifies R_{total}, while the chi-square parameter (χ^2) indicates the accuracy as obtained from the difference between experimental and fitted data.Only fits with a χ^2 of the order of 10^{-4} or lower are considered acceptable. See Experimental Section for acronyms.

Electrode	Cell condition	Equivalent circuit	R_1 [Ω]	R_2 [Ω]	R_{total} [Ω]	χ^2
S@MPAC-73	OCV	$R_e(R_1Q_1)(R_wQ_w)Q_w$	24.8 ± 0.2	–	24.8 ± 0.2	2×10^{-4}
	After 1 CV cycle	$R_e(R_1Q_1)(R_2Q_2)(R_wQ_w)Q_w$	1.0 ± 0.2	5.5 ± 0.3	6.5 ± 0.5	1×10^{-5}
	After 5 CV cycles	$R_e(R_1Q_1)(R_wQ_w)Q_w$	3.2 ± 0.2	–	3.2 ± 0.2	2×10^{-5}
	After 10 CV cycles	$R_e(R_1Q_1)(R_wQ_w)Q_w$	3.5 ± 0.1	–	3.5 ± 0.1	2×10^{-5}
S@MPAC-82	OCV	$R_e(R_1Q_1)(R_wQ_w)Q_w$	26.6 ± 0.5	–	26.6 ± 0.5	7×10^{-5}
	After 1 CV cycle	$R_e(R_1Q_1)(R_wQ_w)Q_w$	1.9 ± 0.1	–	1.9 ± 0.1	2×10^{-5}
	After 5 CV cycles	$R_e(R_1Q_1)(R_wQ_w)Q_w$	2.7 ± 0.1	–	2.7 ± 0.1	4×10^{-5}
	After 10 CV cycles	$R_e(R_1Q_1)(R_wQ_w)Q_w$	3.6 ± 0.1	–	3.6 ± 0.1	6×10^{-5}
S@MPAC-91	OCV	$R_e(R_1Q_1)(R_2Q_2)(R_wQ_w)Q_w$	2.3 ± 0.3	27.2 ± 0.4	29.5 ± 0.7	7×10^{-5}
	After 1 CV cycle	$R_e(R_1Q_1)(R_wQ_w)Q_w$	3.4 ± 0.1	–	3.4 ± 0.1	5×10^{-5}
	After 5 CV cycles	$R_e(R_1Q_1)(R_wQ_w)Q_w$	4.2 ± 0.1	–	4.2 ± 0.1	1×10^{-4}
	After 10 CV cycles	$R_e(R_1Q_1)(R_wQ_w)Q_w$	5.6 ± 0.1	–	5.6 ± 0.1	8×10^{-5}

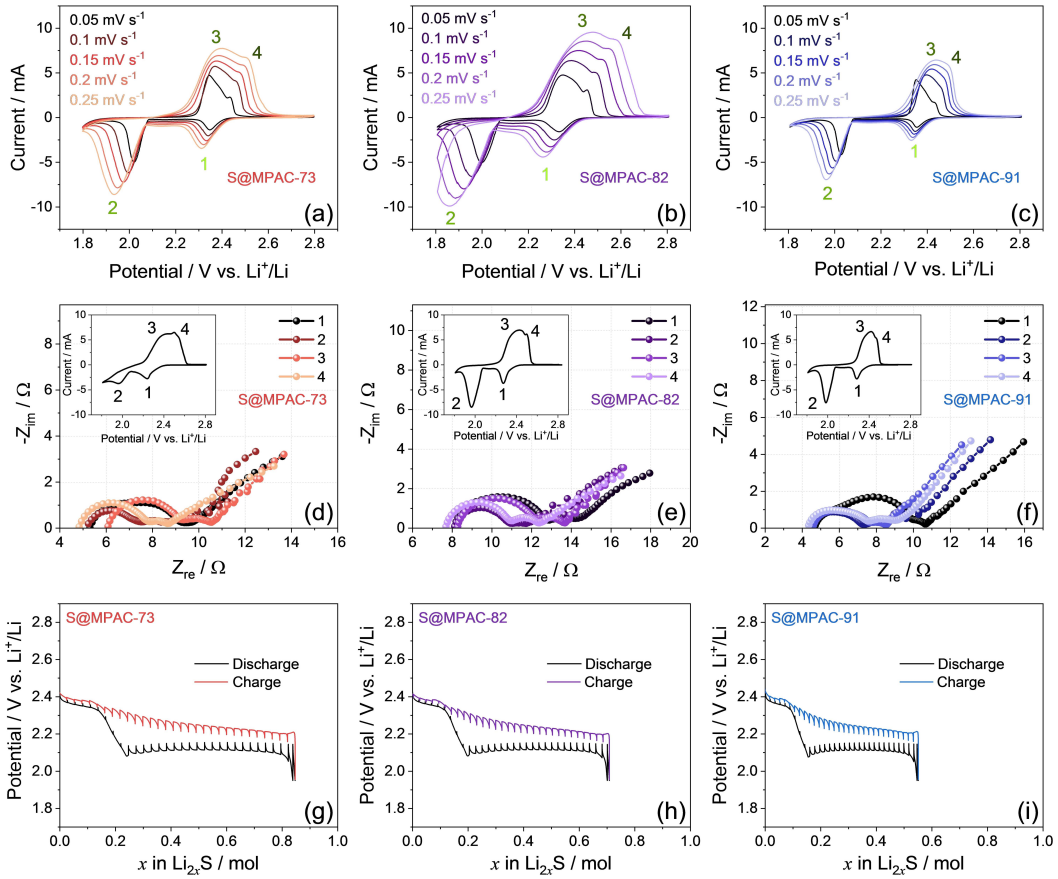

Figure 6. Electrochemical tests performed on Li | DOL : DME, 1 mol kg^{-1} LiTFSI, 1 mol kg^{-1} $LiNO_3$ | cathode cells employing either (a, d, g) S@MPAC-73, (b, e, h) S@MPAC-82 or (c, f, i) S@MPAC-91. In detail: (a–c) Potential profiles related to CV carried out at increasing scan rate, the numbers label the considered potential peaks to calculate D_{Li}^+ through Randles–Sevcik equation [Eq. (1)][81] (D_{CV}) (see also Figure S7 in Supporting Information and Table 3 for specific potentials); (d–f) Nyquist plots recorded by EIS at various states of charge during CV used to calculate D_{Li}^+ by Equation (2)[85], insets show the related voltammograms and reveal the considered SOC (see also Figure S8 in Supporting Information and Table 3 for specific potentials); (g–i) GITT curves reported as potential vs. x (exchanged lithium equivalents n $Li_{2x}S$) used to calculate D_{Li}^+ through GITT equation (4)[87] (see also Figure S9 in Supporting Information and Table 3 for specific potentials). Square current pulses: 167.5 mA g^{-1} (C/10 rate). Time of pulse: 987, 820, and 642 s for S@MPAC-73, S@MPAC-82 and S@MPAC-91, respectively. Potential relaxation step time: 33, 27, and 21 min for S@MPAC-73, S@MPAC-82 and S@MPAC-91, respectively. Cathode sulfur loading: 2.0 mg cm^{-2} with an area of 1.54 cm^{-2}. E/S ratio: 15 µL mg^{-1}. Potential range: 1.95–2.8 V vs. Li^+/Li. See Experimental Section for further details and for acronyms.

$$I_{peak} = 0.4463nFAC\left[\frac{nFvD_{CV}}{RT}\right]^{1/2} \quad (1)$$

where n is the number of exchanged electrons in the electrochemical reaction, F is the Faraday constant (96 485 C mol^{-1}), A is the geometric area of the electrode (1.54 cm^2), C is the estimated Li^+ concentration in the electrode volume [mol cm^{-3}], v is the scan rate [V s^{-1}], D is the diffusion coefficient [cm^2 s^{-1}], R is the gas constant (8.314 J K^{-1} mol^{-1}), and T is the temperature (298 K). According to Equation (1), the D_{Li}^+ values obtained from CV of S@MPAC-73 (Figure 6a), S@MPAC-82 (Figure 6b), and S@MPAC-91 (Figure 6c) in lithium cell, hereafter indicated by D_{CV}, are represented by the linear slopes of the curves reporting I_{peak} and the corresponding $v^{1/2}$, as shown in Figure S7 (Supporting Information), where the labels 1 and 2 correspond to the reduction peaks, while 3 and 4 to the oxidation ones. It is worth noting that the differences between the potential profiles related to CV measurements at constant scan rate (Figure 5) and at increasing scan rate (Figure 6a–c) may be due to the faster activation of the interphase by the lower scan rate employed at the early stages of the latter test compared to the former one, as well as to kinetic limits occurring at the faster scan rates (see Experimental Section).

Furthermore, the analysis of the EIS Nyquist plots of S@MPAC-73 (Figure 6d), S@MPAC-82 (Figure 6e), and S@MPAC-91 (Figure 6f) in the low-frequency region allows the determination of D_{Li}^+ (hereafter indicated by D_{EIS}) at the various states of charge (reported in insets) using Equation (2):[85]

$$D_{EIS} = \frac{1}{2}\left[\frac{RT}{z^2F^2CA\sigma}\right]^2 \quad (2)$$

where R is the gas constant (8.314 J K^{-1} mol^{-1}), T is the temperature (298 K), z is the number of exchanged electrons in the electrochemical reaction, F is the Faraday constant (96485 C mol^{-1}), C is the estimated Li^+ concentration in the electrode volume [mol cm^{-3}], A is the geometric area of the

electrode (1.54 cm^2), and σ is the pre-exponential factor in the equation of the complex impedance (Z^*) vs. frequency (ω) within the semi-infinite diffusion condition, i.e.,

$$Z^*_W = \sigma\omega^{-1/2} - j\sigma\omega^{-1/2} \quad (3)$$

which can be determined by the linear slopes of the plots reported in Figure S8 (Supporting Information) where the real and imaginary components of Z^* (i.e., Z_{re} and Z_{im}, respectively) are reported as function of $\omega^{-1/2}$. It is worth mentioning that all the electrodes reveal the Warburg-type diffusion represented by the line tilted at about 45° in the low-frequency region of the Nyquist graphs reported in Figure 6d–f, which allows the above mentioned linear trend of both Z_{re} and Z_{im} vs. $\omega^{-1/2}$ at approximately constant slope (σ) within the experimental error.

The lithium diffusion coefficient can be also achieved within a wide state of charge (SOC) window by GITT[86] according to a procedure widely used for Li-ion batteries,[87–89] and originally employed herein for Li–S battery. Hence, a galvanostatic titration is hereafter performed according to the details described in the Experimental Section and reported in terms of potential vs. x (exchanged lithium equivalents within $Li_{2x}S$) using S@MPAC-73 (Figure 6g), S@MPAC-82 (Figure 6h), and S@MPAC-91 (Figure 6i) as the working electrode in lithium cell. Indeed, the D_{Li^+}, indicated in this case as D_{GITT}, is calculated by applying Equation (4):[87]

$$D_{GITT} = \frac{4}{\pi}\left[\frac{I^0 V_M}{AF}\frac{dE/dx}{dE/dt^{1/2}}\right]^2, \; t \ll \tau \quad (4)$$

where I^0 [A] is the applied current, V_M is the sulfur molar volume of the electrode (84.48, 80.21, and 80.37 $cm^3 mol^{-1}$ for S@MPAC-73, S@MPAC-82 and S@MPAC-91, respectively), A is the electrode geometric area (1.54 cm^2), F is the Faraday constant (96485 $C mol^{-1}$), τ is the diffusion time employed in the test (s), dE/dx is obtained by derivation of the titration plots in Figure 6d–f, and $dE/dt^{1/2}$ is determined by linear fitting of E vs. $t^{1/2}$ related to each current pulse (with $t \ll \tau$, see Experimental Section), exemplified for the current pulse related to $x = 0.1$ in Figure S9 (Supporting Information). The evolution of the GITT profiles in Figure 6 fully justifies the CV cycles observed previously, however in an almost thermodynamic condition, by showing an initial short reduction plateau at about 2.3 V vs. Li^+/Li during which the S_8 rings break and dissolve into high-order lithium polysulfides and the potential slightly decreases, according to a single-phase transition as indeed observed by the high voltage reduction CV peak (i.e., peak 1).

After a sharp decrease of the potential to about 2.1 V vs. Li^+/Li, the curves show another well-defined two-phase region prolonged until the conversion into short-order lithium polysulfides upon which the potential decreases sharply, thus accounting for the second CV reduction peak (i.e., peak 2). The subsequent oxidation reaction proceeds through specular plateaus, however with an initial process characterized by a certain slope and polarization of about 0.1–0.2 V, along with a potential extending from 2.2 to 2.4 V vs. Li^+/Li (corresponding to CV peak 3), and a final one from about 2.4 to 2.5 V vs. Li^+/Li accounting for the last CV shoulder (peak 4) due to final conversion of the polysulfides into lithium and sulfur.

Interestingly, Figure 6g–i reveals a decrease of the exchanged x value as the content of S in the composite increases, that is, from 0.83 to 0.70 and to 0.55 for S@MPAC-73, S@MPAC-82, and S@MPAC-91, respectively. Table 3 reports the D_{Li^+} values calculated from the data of Figure 6 and the Supporting

Table 3. Li^+ diffusion coefficients (D_{Li^+}) values calculated by applying either Randles–Sevcik equation [Eq. (1)][81] on CV data (D_{CV}, Figure 6a–c, and Figure S7 in Supporting Information), [Eq (2)][85] on EIS analyses (D_{EIS}, Figure 6d–f, and Figure S8 in Supporting Information), and [Eq. (4)][87] on GITT data (D_{GITT}, Figure 6g–i, and Figure S9 in Supporting Information).

Electrode	SOC referred to CV [V vs. Li^+/Li]	D_{CV} [$cm^2 s^{-1}$]	D_{EIS} [$cm^2 s^{-1}$]	SOC referred to GITT [V vs. Li^+/Li]	D_{GITT} [$cm^2 s^{-1}$]
S@MPAC-73	2.30 (discharge peak 1)	3.7×10^{-8}	1.2×10^{-8}	2.35 (discharge region 1)	2.0×10^{-6}
	2.00 (discharge peak 2)	2.8×10^{-8}	3.2×10^{-9}	2.10 (discharge region 2)	7.0×10^{-12}
	2.35 (charge peak 3)	1.8×10^{-8}	3.4×10^{-9}	2.25 (charge region 3)	8.0×10^{-10}
	2.40 (charge peak 4)	1.6×10^{-7}	1.1×10^{-8}	2.40 (charge region 4)	1.7×10^{-7}
S@MPAC-82	2.30 (discharge peak 1)	5.0×10^{-8}	1.4×10^{-8}	2.35 (discharge region 1)	4.0×10^{-6}
	2.00 (discharge peak 2)	3.8×10^{-8}	2.1×10^{-9}	2.10 (discharge region 2)	2.0×10^{-11}
	2.35 (charge peak 3)	3.5×10^{-8}	3.4×10^{-9}	2.25 (charge region 3)	1.0×10^{-10}
	2.40 (charge peak 4)	1.9×10^{-7}	1.1×10^{-8}	2.40 (charge region 4)	2.0×10^{-7}
S@MPAC-91	2.30 (discharge peak 1)	2.1×10^{-8}	6.1×10^{-9}	2.35 (discharge region 1)	3.0×10^{-7}
	2.00 (discharge peak 2)	2.3×10^{-8}	1.4×10^{-9}	2.10 (discharge region 2)	9.0×10^{-12}
	2.35 (charge peak 3	1.3×10^{-8}	2.2×10^{-9}	2.25 (charge region 3)	9.0×10^{-10}
	2.40 (charge peak 4)	1.1×10^{-7}	8.9×10^{-9}	2.40 (charge region 4)	1.0×10^{-7}

Information using the various techniques and related equations, i.e., D_{CV} (Figure 6a–c, Figure S7), D_{EIS} (Figure 6d–f, Figure S8), and D_{GITT} (Figure 6g–i, Figure S9).

Figure 7 illustrates the plots the D_{Li}^+ values according to CV (Figure 7a), EIS (Figure 7b) and GITT (Figure 7c, d) in order to investigate the effects of active material and cell SOC on the diffusion features, as well as to reveal possible influence of the experimental setup used for the study of this key parameter. For a proper comparison, the graphs in Figure 7a, Figure 7b and Figure 7c take into account the four SOC discussed previously, that is, upon first and second reduction processes (1 and 2 in inset) and after the two charge stages (3 and 4 in inset) for CV, EIS and GITT, respectively. Relevantly, the figure shows the dependence of D_{Li}^+ trends and values on the employed technique: hence, D_{CV} ranges between 10^{-7} and 10^{-8} $cm^2 s^{-1}$, as indeed observed in previous reports,[90,91] while D_{EIS} varies with one order of magnitude lower range between 10^{-8} and 10^{-9} $cm^2 s^{-1}$, and D_{GITT} surprisingly shows a much wider interval between 10^{-6} and 10^{-12} $cm^2 s^{-1}$. This notable variability may be ascribed to intrinsic characteristics of the various techniques, as observed in a previous work focusing on insertion materials.[87] Hence, CV reflects transport properties within dynamic conditions during scanning the potential, EIS allows the determination of D_{Li}^+ trends in absence of significant perturbation to mitigate kinetic limits due to lithium transport, while the complex experimental setup of GITT foresees repeated current pulses and cell relaxation with a relevant effect of the employed material and cell. Meanwhile, all the techniques lead to D_{Li}^+ values decreasing by the ongoing of the discharge (from state 1 to 2), due to the formation of the insoluble short-order polysulfides that may hinder the charge transfer, and increasing after charge (state 4) upon the formation of a favorable structure of the electrode in which sulfur or long-order polysulfides are intimately impregnated into the support and the activated carbons.[10,26] Beside similarities, Figure 7 shows that the electrode S@MPAC-91 has mainly lower D_{Li}^+ values compared to S@MPAC-73 and S@MPAC-82, likely due to the higher content of the insulating sulfur. Interestingly, the detailed GITT representation reported in Figure 7d allows the determination of the D_{Li}^+ trend by the whole discharge/charge process of the cell. During discharge, the figure reveals an initial increase of the D_{GITT} from the OCV of the cell, in which crystalline sulfur is the main electrochemically active specie, to x value of 0.125 where the soluble and ion conducting $Li_{0.25}S$ (i.e., Li_2S_8) is formed. The D_{GITT} drops by further discharge to reach a minimum value at x of about 0.5 for S@MPAC-73, 0.4 for S@MPAC-82, and 0.3 for S@MPAC-91, surprisingly raises again when x reaches 0.71, 0.59, and 0.44, and abruptly decreases at the end of discharge with x values of 0.83, to 0.70 and to 0.55, respectively, likely in correspondence to the formation of the most insulating species and the strong polarization at the beginning of the charge. The reverse charge curves initially

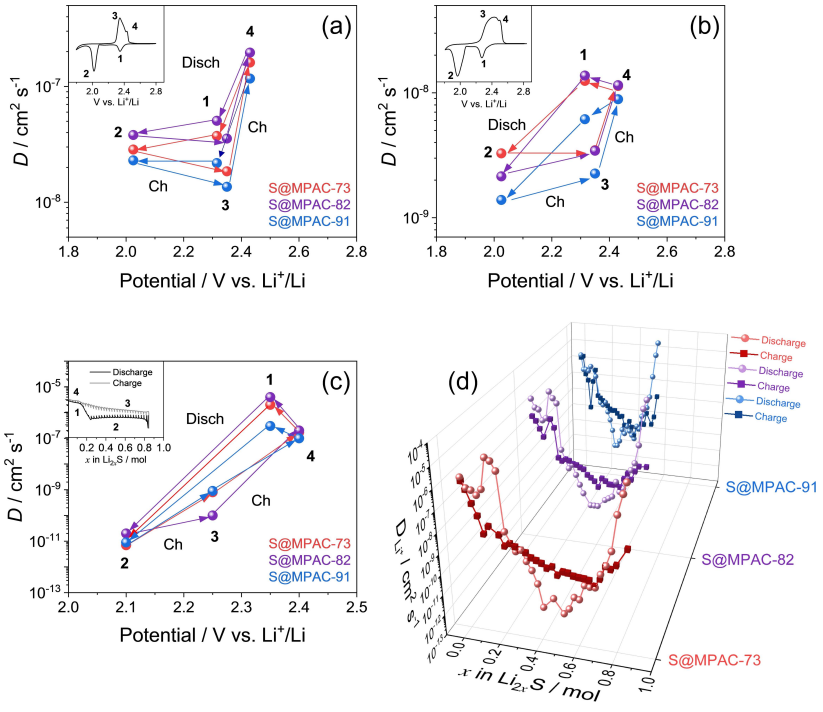

Figure 7. Comparison of the Li^+ diffusion coefficients (D_{Li}^+) calculated through different methods, that is, (a) by Randels–Sevcik equation [Eq. (1)][81] (D_{CV}, see Figure 6a–c, and Figure S7 in Supporting Information), (b) by Equation (2)[85] (D_{EIS}, see Figure 6d–f, and Figure S8 in Supporting Information), and (c) by GITT equation [Eq. (4)][87] by considering selected values obtained by the data of panel (d) showing the trends of the Li^+ diffusion coefficients values as a function of x (exchanged lithium ion in $Li_{2x}S$) during the whole discharge/charge process (see Figure 6g–i, and Figure S9 in Supporting Information). Insets show the regions considered for the calculation of the D values of either voltammograms [panel (a) and (b)] or GITT curves [panel (c)] recorded through electrochemical tests performed on Li | DOL : DME, 1 mol kg^{-1} LiTFSI, 1 mol kg^{-1} $LiNO_3$ | cathode cells employing either the S@MPAC-73, S@MPAC-82 or S@MPAC-91 electrodes. See Table 3 for the selected potentials to calculate the D_{Li}^+ values. See Experimental Section for further details and for acronyms.

evidence a further D_{GITT} decrease, and a subsequent gradual increase until the end of charge back to values comparable to those of the initial discharge states. The D_{Li}^{+} trends observed above indicate a strong interplay between various factors which strongly affect the ions diffusion characteristic, among them: i) the SOC of the cell, ii) the presence of conducting/insulating species in the electrode, iii) the morphology of the formed species during discharge/charge processes, iv) the adopted experimental setup which can lead to possible anisotropy of the results due to the complexity of the Li–S reactions mechanism. It is worth noting that the D_{GITT} values reported in Table 3 for the S@MPAC electrodes are comparable or even higher in the initial stage of discharge and final charged state to those of layered oxides such as LCO, NCO, NCA and NCM (L=Li; C=Co; N=Ni; M=Mn), while higher by orders of magnitude than that measured for $LiFePO_4$, suggesting the S@MPAC electrodes as suitable candidates for application in efficient and high rate Li–S cells.[92]

Figure 8 reports the galvanostatic cycling responses of the three S@MPAC composites performed in lithium cell at currents increasing from C/10 to 2C in order to evaluate the rate capability of the electrodes. The voltage profiles (Figure 8a–c) reveal a shape consisting with the various steps of the redox reactions already described during the CV and GITT discussion, thus accounting for the efficiency of the reversible multi-step conversion process of lithium and sulfur to lithium polysulfides, and the fast kinetics allowed by the inclusion of the activated carbon into the S@MPAC. Indeed, the electrode stands up to a high C-rate (i.e., 2C where 1C = 1675 mA g_S^{-1}) even with a sulfur content increased from 70 wt% (Figure 8a) to 90 wt% (Figure 8c) in the composite, however with capacity decreasing due to the expected polarization increment by raising the current. The comparison of the discharge capacity as a function of the cycle number for the three composites (Figure 8d) further evidences the optimal rate capability of the materials, and shows lower values by carbon content decrease from 30 wt% to 10 wt% and by C-rate raise, with values of 1266, 1224, 1170, 1121, 1010, 928 and 672 mAh g_S^{-1} for S@MPAC-73, 1143, 1095, 1054, 1004, 948, 893, and 672 mAh g_S^{-1} for S@MPAC-82, and 932, 903, 872, 837, 806, 745, and 576 mAh g_S^{-1} for S@MPAC-91 at C/10, C/8, C/5, C/3, C/2, 1C and 2C rate, respectively. This behavior accounts for the key role of the activated carbon added to the sulfur composite in boosting the reaction kinetics, despite a better practical capacity can be achieved by decreasing the carbon content due to higher amount of the active material.[93] The above discussed cells are tested by employing a sulfur loading of about 2 mg cm^{-2} as referred to the geometric area of the electrode (1.54 cm^2), that is, a typical value used for material characterization, which will be subsequently increased to achieve practical cell configuration.[10,26] Notably, the cells using S@MPAC-73, S@MPAC-82, and S@MPAC-91 recover almost the initial discharge capacity value, i.e., 1116, 1048, and 872 mAh g_S^{-1}, respectively, when the current is lowered back to the pristine value of C/10, thus indicating the stability upon the stress triggered by the continuous current raise during the tests.

The cycled electrodes are retrieved upon the rate capability tests from the respective cells (see Experimental Section for details), and studied through SEM-EDS to observe their morphological retention. The SEM images reported in Figure 9 show a homogeneous porous morphology for the S@MPAC-73 (Figure 9a, b), S@MPAC-82 (Figure 9i, j) and S@MPAC-91 (Figure 9q, r) electrodes in line with the stable electrochemical performance displayed in Figure 8. Additional insights are

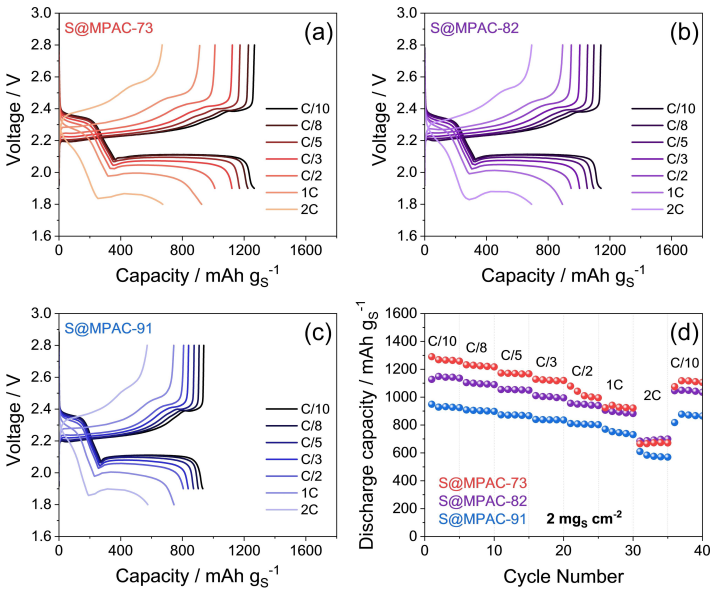

Figure 8. (a–c) Voltage profiles and (d) corresponding cycling trends of rate capability tests carried out on Li | DOL:DME, 1 mol kg^{-1} LiTFSI, 1 mol kg^{-1} $LiNO_3$ | cathode cells employing either (a) S@MPAC-73, (b) S@MPAC-82 or (c) S@MPAC-91 (cathode sulfur loading: 2 mg cm^{-2} with an area of 1.54 cm^{-2}; E/S ratio: 15 µL mg^{-1}). Employed C-rates: C/10, C/8, C/5, C/3, C/2, 1 C, and 2C (1 C = 1675 mA g^{-1}) increased every 5 cycles and lowered back to C/10 after 35 cycles. Voltage ranges: 1.9–2.8 V from C/10 to C/2, and 1.8–2.8 V for 1 C and 2 C. See Experimental Section for acronyms.

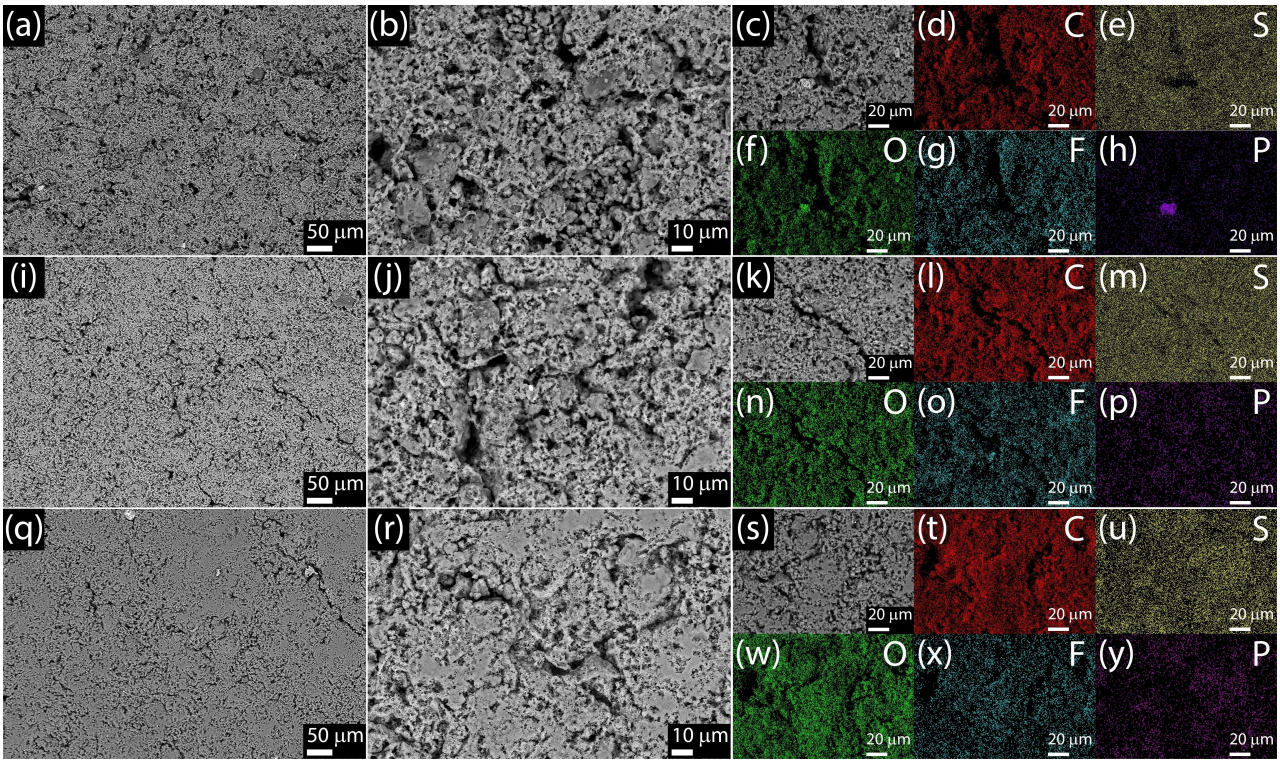

Figure 9. SEM–EDS analyses of the S@MPAC electrodes carried out after rate capability tests in lithium cells (see Figure 8), in particular: (a, b, i, j, q, r) SEM images at various magnification of (a, b) the S@MPAC-73, (i, j) S@MPAC-82 and (q, r) S@MPAC-91 electrodes; (c, k, s) electron images and (d–h, l–p, t–y) corresponding EDS elemental maps of (d, l, t) C, (e, m, u) S, (f, n, w) O, (g, o, x) F and (h, p, y) P related to either (c–h) the S@MPAC-73, (k–p) S@MPAC-82 or (s–y) S@MPAC-91 electrode. See Experimental Section for details of post-mortem electrodes treatment and acronyms.

provided by the EDS elemental maps performed on SEM images (Figure 9c, k and s) revealing that all three electrodes present a uniform distribution of carbon (Figure 9d, l, and t), sulfur (Figure 9e, m and u), and oxygen (Figure 9f, n and w), alongside with fluoride deriving from the PVDF polymer binder used in the electrodes preparation (Figure 9g, o and x) and phosphorous traces ascribable to the MPAC matrix (Figure 9h, p and y). The analyses also show a decrease of surface porosity by sulfur content increase from S@MPAC-73 to S@MPAC-91, in agreement with the SEM images of the sulfur composites in Figure 3.

Hereafter, the S@MPAC composites are tested in lithium cell both by using the sulfur loading of 2 mg cm^{-2} at the high current of 2C (i.e., 3350 mA g$_S^{-1}$) with a test prolonged over 500 cycles, and by increasing the loading to 6 mg cm^{-2} at a lower, but still effective current of C/5 (335 mA g$_S^{-1}$), with outcomes reported in Figure 10. The voltage profiles of the cells using S@MPAC-73 (Figure 10a), S@MPAC-82 (Figure 10b), and S@MPAC-91 (Figure 10c) cycled at 2C rate reveal a relatively high polarization due to the relevant current at the initial cycles, and an activation process during the subsequent ones leading to a progressive increase of the delivered capacity, as indeed expected by the decrease of the cell impedance and polarization discussed in Figure 5 by CV and EIS. Hence, Figure 10d reporting the comparison of the cycling behavior of S@MPAC-73, S@MPAC-82, and S@MPAC-91 at 2C indicates a discharge capacity at the first cycle of about 280, 370 and 490 mAh g$_S^{-1}$ raising to about 870, 850 and 680 mAh g$_S^{-1}$, respectively, while the coulombic efficiency approaches 100% for all cells upon the initial cycling stages. Interestingly, the cell using the electrode with the highest carbon content (i.e., S@MPAC-73) reveals the longer activation step of 60 cycles to reach the maximum capacity with respect to the ones with lower carbon content (i.e., S@MPAC-82 and S@MPAC-91), which show instead an activation prolonged up to 20 cycles as most likely ascribed to a more relevant diffusion process of the sulfur into the carbon expected for the former with respect to the latter by the ongoing of the electrochemical conversion.[76] After the above process, Figure 10d indicates for the Li/S@MPAC-73 cell a higher delivered capacity compared to the ones using S@MPAC-82 and S@MPAC-91, in line with the rate capability test discussed in Figure 8. The slightly better performance in terms of delivered capacity of S@MPAC-73 compared to S@MPAC-82, and of S@MPAC-82 compared to S@MPAC-91 can be ascribed to the progressively increasing carbon content in the sulfur composites that enhances the electrodes conductivity. In addition, the trends of Figure 10d suggest a capacity retention with respect to the maximum delivered value of about 48% for the cell using S@MPAC-91 and 44% for those using S@MPAC-73 and S@MPAC-82 upon the 500 charge/discharge cycles taken into account. The cells with sulfur loading increased up to 6 mg cm^{-2} reveal at C/5 the proper voltage profiles expected for an efficient conversion reaction occurring into S@MPAC-73 (Fig-

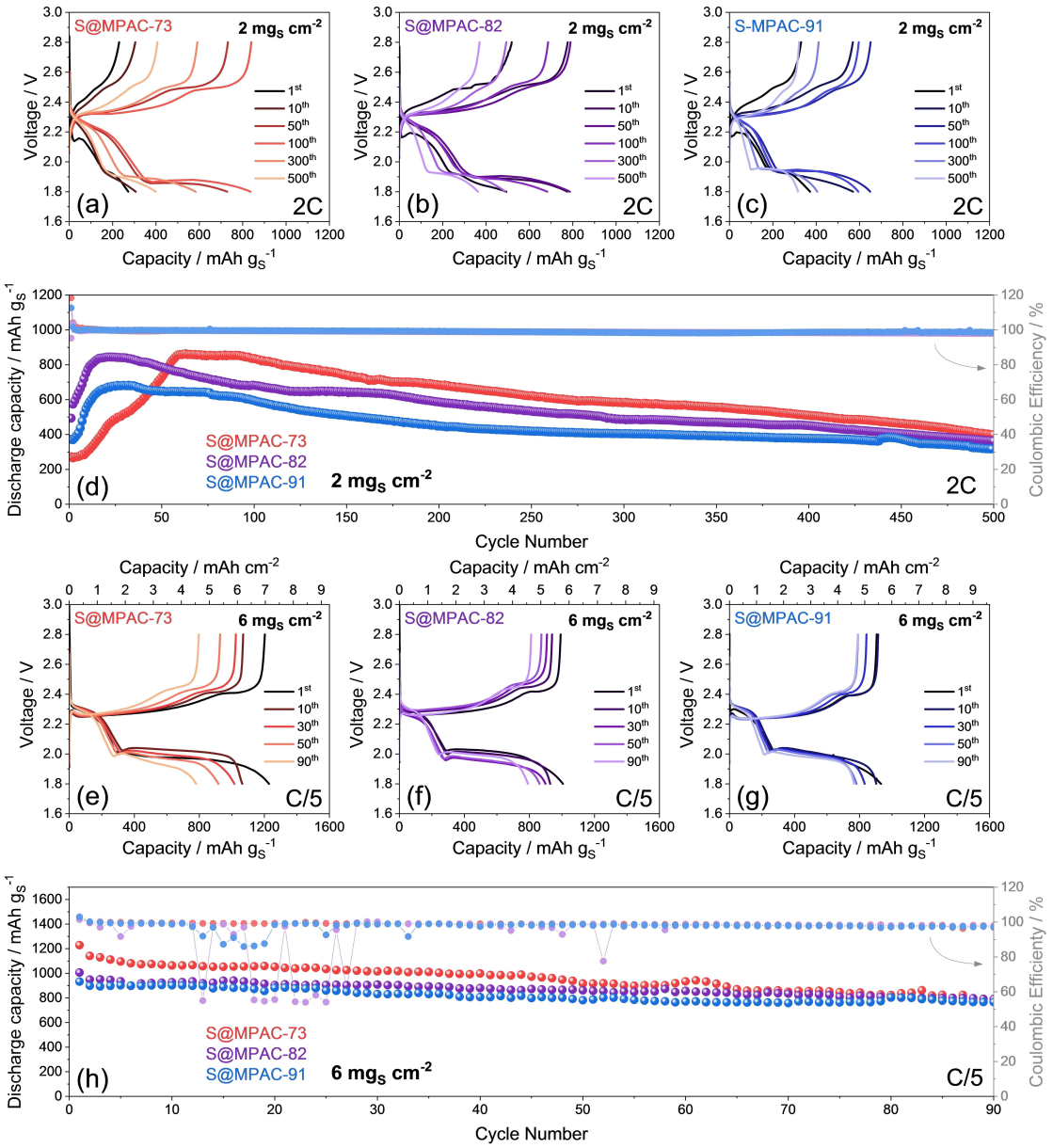

Figure 10. (a–c, e–g) Voltage profiles and (d, h) related cycling trends (coulombic efficiency reported in right *y*-axis) of galvanostatic cycling tests performed on Li | DOL:DME, 1 mol kg^{-1} LiTFSI, 1 mol kg^{-1} $LiNO_3$ | cathode cells employing either the (a, e) S@MPAC-73, (b, f) S@MPAC-82 or (c, g) S@MPAC-91 electrodes at the constant current rate of (a–d) 2C (cathode sulfur loading: 2 mg cm^{-2} with an area of 1.54 cm^{-2}; E/S ratio: 15 µL mg^{-1}) and (e–h) C/5 [cathode sulfur loading: 6 mg cm^{-2} with an area of 1.54 cm^{-2}; E/S ratio: 10 µL mg^{-1}, see areal capacity in mAh cm^{-2} in top *x*-axis in panels (e–f)]. Voltage ranges: 1.8–2.8 V. See Experimental Section for acronyms.

ure 10e), S@MPAC-82 (Figure 10f) and S@MPAC-91 (Figure 10g), with limited polarization, initial capacities of about 1220, 1020 and 940 mAh g$_S^{-1}$, and final values of about of about 780, 790 and 760 mAh g$_S^{-1}$ upon 90 cycles, respectively. Moreover, the profiles of Figure 10e–g indicate a notable value of the areal capacity [mAh cm^{-2}] ranging from 4.5 to 7 mAh cm^{-2} for the various electrodes. This performance can actually reflect an improved volumetric energy density value.

Therefore, Figure 10h accounts for a capacity retention increasing from 65% for S@MPAC-73, to 79% for S@MPAC-82, and to 80% for S@MPAC-91, as most likely ascribed to a better electrode/electrolyte interphase triggered by the optimal cell composition in terms of overall S to C ratio and E/S ratio, the latter decreased from 15 to 10 µL mg$_S^{-1}$ as the sulfur loading is increased from 2 to 6 mg cm^{-2}. The above decrease of the E/S ratio can lead to advantages in term of cell energy density and scalability, that are more relevant in Li–S cell reported in Figure S10 (Supporting Information) using the S@MPAC-91 electrode with a sulfur loading increased to 11 mg cm^{-2} and E/S ratio decreased to 5 µL mg$_S^{-1}$. The cell is cycled at C-rate lowered to C/20 in order to avoid excessive ohmic drop due to the challenging current (1C = 18 mA cm^{-2}), and allow the

operation according to the above discussed increase of the capacity upon cycling to achieve an areal value of 5 mAh cm^{-2} (i.e., about 600 mAh g_S^{-1}). It is worth mentioning that the challenging conditions of the tests can occasionally promote partial decrease of the coulombic efficiency due to micro-dendrites formation (in particular for S@MPAC-82 in Figure 10h), however without significant effects on the cell performances as demonstrated by the satisfactory cycle life achieved by the three electrodes. Such a promising result suggests the material as viable candidate for application in effective Li–S cell with improved practical performance. Further studies in different cell configuration such as the pouch cell one can further proof the actual applicability of this system, however additional challenges ascribed to the cell assembly and geometry should be certainly taken into account.[94]

Conclusions

We reported herein a study of the most relevant features with particular focus on the diffusional characteristics of a Li–S battery using an activated carbon derived from biomass (MPAC) with a high surface area and a well-defined microporous structure, suited to accommodate high active material content and allow the preparation of composites with sulfur amount of 70 wt% (S@MPAC-73), 80 wt% (S@MPAC-82), and 90 wt% (S@MPAC-91). The tests indicated for the materials adequate structure, suitable morphology and chemical nature, and the absence of reactive impurities. These features allowed an efficient electrochemical process in Li–S cell, with reduction potentials of 2.3 and 1.9 V vs. Li^+/Li reversed at 2.1 and 2.5 V vs. Li^+/Li during oxidation, and a limited impedance decreasing from tens to units of ohms upon CV due to a favorable activation process occurring by repeated sulfur electrode dissolution and subsequent deposition. Most relevantly, the diffusion characteristics of the lithium ions have been determined using the three electrodes in the Li–S system at various SOC, and throughout different electrochemical techniques, that is, CV, EIS, and GITT. The study evidenced the dependence of D_{Li^+} on the employed technique, and indicated D_{CV} ranging between 10^{-7} and 10^{-8} $cm^2 s^{-1}$, D_{EIS} between 10^{-8} and 10^{-9} $cm^2 s^{-1}$, and D_{GITT} between 10^{-6} and 10^{-12} $cm^2 s^{-1}$. These trends accounted for the complex interplay between the SOC, the electrode nature, structure and morphology, as well as the adopted experimental setup in determining the diffusional parameters of the cell. The study has shown for all electrodes the decrease of the D_{Li^+} at the end of the discharge when insulating short-order polysulfides are formed, and its increase back as the high-order ones are achieved by charge, with values of the same order or even higher compared to the most performing commercial materials projected for Li-ion battery. The electrodes revealed in lithium cell a capacity ranging from 1266 to 672 mAh g_S^{-1} for S@MPAC-73, from 1143 to 672 mAh g_S^{-1} for S@MPAC-82, and from 932 to 576 mAh g_S^{-1} for S@MPAC-91 at current increasing from C/10 to 2C, respectively, thus accounting for the actual applicability of the carbon precursor even by increasing the sulfur content in the composite to values as high as 90 wt%. Prolonged tests of S@MPAC-73, S@MPAC-82, and S@MPAC-91 in lithium cells with sulfur loading of 2 mg cm^{-2} and E/S ratio of 15 μL mg_S^{-1} at 2C rate evidenced an activation trend with a maximum capacity of 870, 850 and 680 mAh g_S^{-1}, retained for about 45% over 500 cycles, instead cells cycled at C/5 using electrodes with loadings increased up to 6 mg cm^{-2} and E/S ratio limited to 10 μL mg_S^{-1} have shown a maximum capacity of about 1200, 1000 and 950 mAh g_S^{-1} (corresponding to about 5.5–7 mAh cm^{-2}) retained upon 90 cycles over 65, 79 and 80%, respectively. Even more practical Li–S cell has been achieved using the most concentrated electrode (S@MPAC-91) with a sulfur loading increased up to 11 mg cm^{-2} and an E/S ratio decreased to 5 μL mg_S^{-1} with a promising geometric surface capacity of 5 mAh cm^{-2}. These findings provide key information on the diffusional characteristics of the lithium sulfur cell which may actually help in rationalizing such a challenging and complex energy storage system.

Experimental Section

Carbon synthesis

Mango pits were cut into pieces with a size of 1–2 cm, washed with distilled water under stirring in ambient temperature for 3 h and then dried in an oven at 120 °C in air overnight. The dried pieces were ground in a planetary ball mill (PM100 model, Retsch) at 300 rpm for 30 min using a 125 mL grinding jar with 8 stainless steel balls (10 mm diameter). Then, the obtained powder was impregnated with a solution of H_3PO_4 (85%, Panreac) in a mass ratio of 1:1 and subsequently heated in a hot plate under stirring at 85 °C for 3 h until a solid paste was obtained, which was dried at 120 °C in overnight. The impregnated product was ground again in the planetary ball mill at 300 rpm for 30 min, heated at 10 °C min^{-1} in a tubular furnace (ST-11 model, Hobersal) to 700 °C and calcinated for 2 h under a N_2 atmosphere (flow rate of 50 mL min^{-1}). To remove the impurities, the sample was subsequently treated with a solution of 3 M HCl (37%, Panreac) and heated in a hot plate under stirring at 80 °C for 3 h and then washed with distilled water until neutral pH was achieved. The resulting powder was dried in an oven at 120 °C for one day. The activated carbon obtained from mango pit was indicated in the work using the acronym MPAC.

Sulfur composites preparation

MPAC was dried in a vacuum glass oven (Büchi) at 120 °C for 3 h and then mixed with elemental sulfur (≥99.5%, Riedel-de Haën) in different S/C mass ratios, i.e., 70:30, 80:20 and 90:10. The mixtures were then heated in a silicon oil bath at 120 °C under magnetic stirring until complete melting of sulfur, and subsequently quenched to room temperature until sulfur solidification and ground in an agate mortar. The above composites were indicated with the acronyms S@MPAC-73, S@MPAC-82 and S@MPAC-91, respectively.

Materials characterization

X-ray diffraction (XRD) patterns of the carbon and the respective composites were obtained with a D8 Advance (Bruker) diffractometer equipped with a $Cu_{K\alpha}$ source (8.05 keV) in the range of 2θ between 10° and 90° with a step size of 0.02° and a scan rate of

10 s per step. Raman spectra of the carbon was collected via an alpha500 WITec confocal Raman spectrometer with a frequency doubled Nd:YAG (532.06 nm) laser excitation focused on the sample using a 20×/0.4 Zeiss objective with an integration time of 1s by accumulating a total of 10 spectra. Thermogravimetric analysis (TGA) measurements were performed through a TGA 2 Mettler-Toledo instrument in the temperature range of 25–800 °C with a heating rate of 5 °C min^{-1} under 100 mL min^{-1} flux of O_2 for the carbon and in the temperature range of 25–700 °C with the same heating rate and flow under N_2 for the sulfur composites. The N_2 adsorption-desorption isotherm of the carbon was obtained with an ASAP 2020 Micromeritics porosimeter using nitrogen gas as adsorbate. The specific surface area was calculated using the Brunauer-Emmett-Teller (BET) method based on nitrogen adsorption isotherm at the temperature of liquid nitrogen (77 K). The pore size distribution (PSD) was calculated using density functional theory (DFT). The scanning electron microscopy (SEM) images were obtained with a Zeiss EVO 40 microscope using a LaB_6 thermionic electron gun. Energy dispersive X-ray spectroscopy (EDS) microanalysis were obtained in a JEOL JSM-7800F microscope equipped with a X-ACT Cambridge Instruments analyzer. The polysulfides retention ability of the MPAC was investigated by UV/Vis spectroscopy and X-ray photoelectron spectroscopy (XPS). A 0.1 M solution of Li_2S_6 lithium polysulfide was prepared according to a modified synthetic procedure.[95] Lithium sulfide (Li_2S, 99.98% trace metals basis, Sigma-Aldrich) and sulfur (Solvay) powders were dried under vacuum at 40 °C for 72 h and subsequently mixed in a 1:5 molar ratio in an argon sealed flask. The mixture was dispersed into a 1:1 *v/v* solution of 1,3-dioxolane (DOL, 99.8% anhydrous with ca. 75 ppm BHT as inhibitor, Sigma-Aldrich) and 1,2-dimethoxyethane (DME, 99.5% anhydrous, inhibitor-free, Sigma-Aldrich) previously stirred at 60 °C for 24 h in an Ar-filled glovebox (I-Lab 4GB, H_2O and $O_2 < 1$ ppm). Afterwards, the Li_2S_6 solution was diluted with the DOL/DME mixture to reach a concentration of 5 mM, and 5 mL of the new Li_2S_6 solution was added to 25 mg of MPAC carbon host. After 6 h of aging, the obtained precipitated was filtered and dried under vacuum. XPS tests were carried out on the pristine 5 mM Li_2S_6 solution and on the MPAC sample aged in contact with Li_2S_6, while UV/Vis measurements were performed on the pristine 5 mM Li_2S_6 solution and the one treated with the MPAC. Prior to the tests, DOL and DME solvents were dried under molecular sieves (0.3 nm, rods, size 1.6 mm (1/16 in.), Sigma-Aldrich) to reduce the H_2O content and the pristine MPAC sample was dried under vacuum at 120 °C overnight. The UV/Vis spectra were recorded by using 3 mL micro-quartz cuvettes in a double beam spectrophotometer Zuzi 4260/50 model equipped with two detectors in the visible wavelength region from 350 nm to 600 nm. XPS spectra of the MPAC and S@MPAC composites were recorded with a PHOBIOS 150 MCD SPECS spectrometer with a monochromatic $Mg_{K\alpha}$ (1253.6 eV) radiation and a multichannel detector in a chamber able to reach a pressure of 4×10^{-9} mbar. XPS spectra aimed to evaluate the polysulfides adsorption of the MPAC were obtained by using a Physical Electronic PHI VERSAPROBE spectrometer with monochromatic $Al_{K\alpha}$ radiation (1486.6, 15 kV, 1253.6 eV) and a multichannel detector. The energy scale of the spectrometer was calibrated using the $Cu2p_{3/2}$, $Ag3d_{5/2}$, and $Au4f_{7/2}$ photoelectron lines at binding energies of 932.7, 368.3 and 84.0 eV, respectively. The spectra were recorded in the constant pass energy mode at 29.35 eV, using a 200 μm diameter analysis area. The samples were secured on a sample holder with adhesive tape and kept under high vacuum in the preparation chamber before transfer to the analysis chamber. The residual pressure in the analysis chamber was kept below 2.0×10^{-7} Pa during the acquisition of the spectra. Binding energy values were referred to the C1s peak at 284.8 eV. The error in the binding energy was estimated to be about ±0.1 eV.

Electrode preparation

The electrodes were prepared by mixing in an agate mortar the S@MPAC-73, S@MPAC-82 and S@MPAC-91 composites, respectively, with polyvinylidene fluoride (PVDF 6020, Solef) as the binder and carbon black (Super P, Timcal) as the conducting agent in a weight ratio of 80:10:10 using *N*-methyl-2-pyrrolidone (NMP, Sigma-Aldrich) as the solvent. The obtained slurries were cast on carbon-cloth foils (GDL ELAT LT1400, MTI Corp.) through the doctor blade method (MTI Corp.). The coated films were heated on a hot plate at 50 °C in air for 3 h. The electrodes were cut into 14 mm diameter disks (1.54 cm^2 area) and inserted into a vacuum glass oven (Büchi) at 35 °C overnight before cell assembly in an argon-filled glovebox (MBraun, H_2O and $O_2 < 1$ ppm). The electrodes were prepared into three batches with sulfur loadings of 2.0, 6.0 and 11.0 mg cm^{-2}.

Cell assembly, electrolyte preparation, electrochemical measurements and post-mortem analyses

The sulfur electrodes were assembled into a CR2032 coin-cell configuration (MTI Corp.) in an argon-filled glovebox (MBraun, H_2O and $O_2 < 1$ ppm) with a lithium metal disk as the counter and reference electrode (14 mm diameter), and a polyethylene separator (Celgard 2400, 16 mm diameter) soaked with the electrolyte solution. The electrolyte/sulfur (E/S) ratio was of 15, 10 and 5 μL mg^{-1} for sulfur loading of 2.0, 6.0 and 11.0 mg cm^{-2}, respectively. The electrolyte solution was prepared by dissolving lithium bis(trifluoromethanesulfonyl)imide (LiTFSI, 99.95% trace metals basis, Sigma-Aldrich) and lithium nitrate ($LiNO_3$, 99.99% trace metals basis, Sigma-Aldrich) salts in a mixture of DOL and DME solvents (1:1, *w/w* ratio). The final concentration of each salt in the electrolyte solution was of 1 mol kg^{-1} with respect to the weight of solvent (i.e., DOL:DME). Previously, LiTFSI and $LiNO_3$ salts were dried at 110 °C under vacuum in glass oven (Büchi) for 3 days, while DOL and DME solvents were dried under molecular sieves (3 Å, rod, size 1/16 in., Honeywell Fluka) and the residual moisture was measured using a Karl Fischer 899 Coulometer (Metrohm) until the water content was lower than 10 ppm. Cyclic voltammetry (CV) and electrochemical impedance spectroscopy (EIS) measurements were recorded on VersaSTAT MC Princeton Applies Research (PAR-AMETEK) analyzer. The CV was carried out within a potential range of 1.8–2.8 V vs. Li^+/Li using a constant scan rate of 0.1 mV s^{-1}, while the EIS measurements were recorded at open circuit volage (OCV) condition and after 1, 5 and 10 CV cycles in the frequency range from 500 kHz to 100 mHz by using a 10 mV alternate voltage signal amplitude. The resulting Nyquist plots were analyzed with the non-linear least squares (NLLS) fitting method using the Boukamp software (χ^2 values considered suitable in the order of 10^{-4} or lower).[83,84] The CV measurements for the lithium-ion diffusion coefficients (D_{Li}) calculations were performed in the same potential range and under different scan rates, that is, 0.05, 0.1, 0.15, 0.2, and 0.25 mV s^{-1}. The EIS measurements for D_{Li^+} calculations were recorded at the same frequency range within different electrode state of charge (SOC) obtained by linear sweep voltammetry (LSV) after a first CV activation cycle recorded at the same potential range and under a constant scan rate of 0.05 mV s^{-1}. Galvanostatic intermittent titration technique (GITT) measurements were performed using a MACCOR series 4000 battery tester system after three activation cycles at C/10 (1C = 1675 mA g_S^{-1}) in the voltage range of 1.95–2.8 V. The titrations were carried out by applying square current pulses of 167.5 mA g^{-1} during $t = 987$, 820, and 642 s for S@MPAC-73, S@MPAC-82, and S@MPAC-91 electrodes, respectively, followed by potential relaxation steps of 33, 27, and 21 min at the reached SOC. Galvanostatic discharge-charge cycling tests were performed using a MACCOR series 4000 battery tester. Electrodes with a sulfur loading of 2 mg cm^{-2} were tested within

the current rates from C/10 to 2C (1C = 1675 mA g_S^{-1}). In detail, rate capability measurements were performed under current rates of C/10, C/8, C/5, C/3, C/2, 1C, and 2C increasing every 5 cycles, then returning to C/10 for the last 5 cycles. Voltage ranges of 1.9–2.8 V were used from C/10 to C/2 and of 1.8–2.8 V for 1C and 2C during the rate capability test. Afterwards, the cells were disassembled and the electrodes retrieved, washed with DME solvent, dried under vacuum for 30 min at room temperature, and investigated through SEM-EDS analyses by exploiting a Zeiss EVO 40 microscope using a LaB_6 thermionic electron gun (SEM) coupled with a X-ACT Cambridge Instruments analyzer (EDS). Galvanostatic measurements were also carried out for the electrodes with a sulfur loading of 2.0 mg cm^{-2} over 500 cycles at 2C current rate within the voltage range of 1.8–2.8 V. Electrodes with a sulfur loading of 6.0 mg cm^{-2} were tested over 90 cycles at a constant current rate of C/5 rate in a voltage range of 1.8–2.8 V, and electrodes with a sulfur loading of 11.0 mg cm^{-2} were tested over 45 cycles at a constant current rate of C/20 in a voltage range of 1.7–2.8 V. All the electrochemical measurements were performed at the controlled room temperature (25 °C).

Acknowledgements

This project/work has received funding from the European Union's Horizon 2020 research and innovation programme Graphene Flagship under grant agreement No 881603. Likewise, this research was funded by Ministerio de Ciencia e Innovación (Project PID2020-113931RB–I00 & PDC2021-120903-I00) and Junta de Andalucía (Project P20_00432 and Group FQM-175). The authors also thank grant "Fondo di Ateneo per la Ricerca Locale (FAR) 2020", University of Ferrara, and the collaboration project "Accordo di Collaborazione Quadro 2015" between University of Ferrara (Department of Chemical and Pharmaceutical Sciences) and Sapienza University of Rome (Department of Chemistry). The authors acknowledge the SCAI of the University of Malaga for recording of the XPS spectra and Prof. Enrique Rodriguez Castellon at the same university for the UV-Vis adsorption spectra fitting. Open Access funding provided by Università degli Studi di Ferrara within the CRUI-CARE Agreement.

Conflict of Interest

The authors declare no conflict of interest.

Data Availability Statement

The data that support the findings of this study are available in the supplementary material of this article.

Keywords: activated carbon · diffusion process · fast-kinetics · high-energy · Li–S batteries

[1] C. D. Thomas, A. Cameron, R. E. Green, M. Bakkenes, L. J. Beaumont, Y. C. Collingham, B. F. N. Erasmus, M. F. De Siqueira, A. Grainger, L. Hannah, L. Hughes, B. Huntley, A. S. Van Jaarsveld, G. F. Midgley, L. Miles, M. A Ortega-Huerta, A. Townsend Peterson, O. L. Phillips, S. E. Williams, *Nature* **2004**, *427*, 145.
[2] J. Neubauer, E. Wood, *J. Power Sources* **2014**, *259*, 262.
[3] D. Di Lecce, R. Verrelli, J. Hassoun, *Green Chem.* **2017**, *19*, 3442.
[4] A. Manthiram, Y. Fu, S.-H. Chung, C. Zu, Y.-S. Su, *Chem. Rev.* **2014**, *114*, 11751.
[5] G. Zhang, Z.-W. Zhang, H.-J. Peng, J.-Q. Huang, Q. Zhang, *Small Methods* **2017**, *1*, 1700134.
[6] Z. W. Seh, Y. Sun, Q. Zhang, Y. Cui, *Chem. Soc. Rev.* **2016**, *45*, 5605.
[7] R. Fang, S. Zhao, Z. Sun, D.-W. Wang, H.-M. Cheng, F. Li, *Adv. Mater.* **2017**, *29*, 1606823.
[8] Y. Chen, T. Wang, H. Tian, D. Su, Q. Zhang, G. Wang, *Adv. Mater.* **2021**, *33*, 2003666.
[9] L. Carbone, S. Greenbaum, J. Hassoun, *Sustain. Energy Fuels* **2017**, *1*, 228.
[10] V. Marangon, D. Di Lecce, D. J. L. Brett, P. R. Shearing, J. Hassoun, *J. Energy Chem.* **2022**, *64*, 116.
[11] V. Marangon, D. Di Lecce, F. Orsatti, D. J. L. Brett, P. R. Shearing, J. Hassoun, *Sustain. Energy Fuels* **2020**, *4*, 2907.
[12] S. Drvarič Talian, J. Moškon, R. Dominko, M. Gaberšček, *ACS Appl. Mater. Interfaces* **2017**, *9*, 29760.
[13] C. Liedel, *ChemSusChem* **2020**, *13*, 2110.
[14] H. Wu, J. Mou, L. Zhou, Q. Zheng, N. Jiang, D. Lin, *Electrochim. Acta* **2016**, *212*, 1021.
[15] L. Fan, Z. Li, W. Kang, B. Cheng, *Renewable Energy* **2020**, *155*, 309.
[16] S. S. Zhang, *J. Power Sources* **2016**, *322*, 99.
[17] D. Di Lecce, V. Marangon, H.-G. Jung, Y. Tominaga, S. Greenbaum, J. Hassoun, *Green Chem.* **2022**, *24*, 1021.
[18] V. Marangon, D. Di Lecce, L. Minnetti, J. Hassoun, *ChemElectroChem* **2021**, *8*, 3971.
[19] A. Benítez, A. Caballero, J. Morales, J. Hassoun, E. Rodríguez-Castellón, J. Canales-Vázquez, *Nano Res.* **2019**, *12*, 759.
[20] F. Jin, S. Xiao, L. Lu, Y. Wang, *Nano Lett.* **2016**, *16*, 440.
[21] X. Zhao, M. Kim, Y. Liu, H.-J. Ahn, K.-W. Kim, K.-K. Cho, J.-H. Ahn, *Carbon* **2018**, *128*, 138.
[22] S. Liu, X. Hong, D. Wang, Y. Li, J. Xu, C. Zheng, K. Xie, *Electrochim. Acta* **2018**, *279*, 10.
[23] S. Choudhury, D. Fischer, P. Formanek, F. Simon, M. Stamm, L. Ionov, *Polymer* **2018**, *151*, 171.
[24] L. Zhang, Y. Wang, Z. Niu, J. Chen, *Carbon* **2019**, *141*, 400.
[25] R. Xiao, K. Chen, X. Zhang, Z. Yang, G. Hu, Z. Sun, H.-M. Cheng, F. Li, *J. Energy Chem.* **2021**, *54*, 452.
[26] D. Di Lecce, V. Marangon, W. Du, D. J. L. Brett, P. R. Shearing, J. Hassoun, *J. Power Sources* **2020**, *472*, 1.
[27] L. Zhou, H. Li, X. Wu, Y. Zhang, D. L. Danilov, R.-A. Eichel, P. H. L. Notten, *ACS Appl. Energ. Mater.* **2019**, *2*, 8153.
[28] Y. Lu, Y. Jia, S. Zhao, L. Chen, Y. Su, F. Wu, J. Li, X. Liu, S. Chen, R. Chen, *ACS Appl. Energ. Mater.* **2019**, *2*, 4151.
[29] Y. Mao, G. Li, Y. Guo, Z. Li, C. Liang, X. Peng, Z. Lin, *Nat. Commun.* **2017**, *8*, 14628.
[30] Z. Li, Z. Xiao, S. Wang, Z. Cheng, P. Li, R. Wang, *Adv. Funct. Mater.* **2019**, *29*, 1902322.
[31] Q. Pang, X. Liang, C. Y. Kwok, L. F. Nazar, *J. Electrochem. Soc.* **2015**, *162*, A2567.
[32] L. Zhou, D. L. Danilov, R. Eichel, P. H. L. Notten, *Adv. Energy Mater.* **2021**, *11*, 2001304.
[33] L. Borchardt, M. Oschatz, S. Kaskel, *Chem. Eur. J.* **2016**, *22*, 7324.
[34] L. Carbone, T. Coneglian, M. Gobet, S. Munoz, M. Devany, S. Greenbaum, J. Hassoun, *J. Power Sources* **2018**, *377*, 26.
[35] B. Khiari, M. Jeguirim, L. Limousy, S. Bennici, *Renewable Sustainable Energy Rev.* **2019**, *108*, 253.
[36] N. Moreno, A. Caballero, L. Hernán, J. Morales, *Carbon* **2014**, *70*, 241.
[37] C. Hernández-Rentero, R. Córdoba, N. Moreno, A. Caballero, J. Morales, M. Olivares-Marín, V. Gómez-Serrano, *Nano Res.* **2018**, *11*, 89.
[38] F. Li, F. Qin, K. Zhang, J. Fang, Y. Lai, J. Li, *J. Power Sources* **2017**, *362*, 160.
[39] A. Y. Tesio, J. L. Gómez-Cámer, J. Morales, A. Caballero, *ChemSusChem* **2020**, *13*, 3439.
[40] J. Ren, Y. Zhou, H. Wu, F. Xie, C. Xu, D. Lin, *J. Energy Chem.* **2019**, *30*, 121.
[41] M. Xiang, Y. Wang, J. Wu, Y. Guo, H. Wu, Y. Zhang, H. Liu, *Electrochim. Acta* **2017**, *227*, 7.
[42] Y. Cui, Q. Zhang, J. Wu, X. Liang, A. P. Baker, D. Qu, H. Zhang, H. Zhang, X. Zhang, *J. Power Sources* **2018**, *378*, 40.
[43] M. Zhong, J. Guan, J. Sun, H. Guo, Z. Xiao, N. Zhou, Q. Gui, D. Gong, *Electrochim. Acta* **2019**, *299*, 600.

[44] M. Olivares-Marín, C. Fernández-González, A. Macías-García, V. Gómez-Serrano, *Carbon* **2006**, *44*, 2347.
[45] H. Wu, Y. Deng, J. Mou, Q. Zheng, F. Xie, E. Long, C. Xu, D. Lin, *Electrochim. Acta* **2017**, *242*, 146.
[46] T.-Z. Hou, X. Chen, H.-J. Peng, J.-Q. Huang, B.-Q. Li, Q. Zhang, B. Li, *Small* **2016**, *12*, 3283.
[47] V. Do, Deepika, M. S. Kim, M. S. Kim, K. R. Lee, W. il Cho, *ACS Appl. Mater. Interfaces* **2019**, *11*, 11431.
[48] A. Benítez, M. González-Tejero, Á. Caballero, J. Morales, *Materials* **2018**, *11*, 1428.
[49] A. Benítez, J. Morales, Á. Caballero, *Nanomaterials* **2020**, *10*, 840.
[50] V. Marangon, C. Hernández-Rentero, M. Olivares-Marín, V. Gómez-Serrano, Á. Caballero, J. Morales, J. Hassoun, *ChemSusChem* **2021**, *14*, 3333.
[51] S. Zhang, M. Zheng, Z. Lin, R. Zang, Q. Huang, H. Xue, J. Cao, H. Pang, *RSC Adv.* **2016**, *6*, 39918.
[52] FAOSTAT, *Crops and livestock products*, **2022**.
[53] L. Barbosa, F. Luna-Lama, Y. González Peña, A. Caballero, *ChemSusChem* **2020**, *13*, 838.
[54] J. C. Arrebola, A. Caballero, L. Hernán, J. Morales, V. Gómez-Serrano, *J. Electrochem. Soc.* **2010**, *157*, A791.
[55] A. Jorio, E. H. M. Ferreira, M. V. O. Moutinho, F. Stavale, C. A. Achete, R. B. Capaz, *Phys. Status Solidi B* **2010**, *247*, 2980.
[56] C. Hernández-Rentero, O. Vargas, A. Caballero, J. Morales, F. Martín, *Electrochim. Acta* **2016**, *222*, 914.
[57] A. Benítez, D. Di Lecce, G. A. Elia, Á. Caballero, J. Morales, J. Hassoun, *ChemSusChem* **2018**, *11*, 1512.
[58] J. Xu, J. Shui, J. Wang, M. Wang, H.-K. Liu, S. X. Dou, I.-Y. Jeon, J.-M. Seo, J.-B. Baek, L. Dai, *ACS Nano* **2014**, *8*, 10920.
[59] T. A. Zegeye, M.-C. Tsai, J.-H. Cheng, M.-H. Lin, H.-M. Chen, J. Rick, W.-N. Su, C.-F. J. Kuo, B.-J. Hwang, *J. Power Sources* **2017**, *353*, 298.
[60] B. Xu, S. Qi, F. Li, X. Peng, J. Cai, J. Liang, J. Ma, *Chin. Chem. Lett.* **2020**, *31*, 217.
[61] C. D. Wanger, W. M. Riggs, L. E. Davis, J. F. Moulder, G. E. Muilenberg, *Perkin-Elmer Corp., Physical Electronics Division, Eden Prairie,* Minnesota, USA, **1979**, 190pp.
[62] G. Zhou, E. Paek, G. S. Hwang, A. Manthiram, *Nat. Commun.* **2015**, *6*, 7760.
[63] J. Qu, C. Geng, S. Lv, G. Shao, S. Ma, M. Wu, *Electrochim. Acta* **2015**, *176*, 982.
[64] H. Zheng, Q. Cao, M. Zhu, D. Xu, H. Guo, Y. Li, J. Zhou, *J. Mater. Chem. A* **2021**, *9*, 10120.
[65] J. Deng, M. Li, Y. Wang, *Green Chem.* **2016**, *18*, 4824.
[66] E. Antolini, *Renewable Sustainable Energy Rev.* **2016**, *58*, 34.
[67] J. Wu, Q. Zhang, M. Li, J. Yan, Y. Zhang, J. Liu, Y. Wu, *RSC Adv.* **2019**, *9*, 15715.
[68] M. J. Klein, K. Goossens, C. W. Bielawski, A. Manthiram, *J. Electrochem. Soc.* **2016**, *163*, A2109.
[69] Q. Pang, J. Tang, H. Huang, X. Liang, C. Hart, K. C. Tam, L. F. Nazar, *Adv. Mater.* **2015**, *27*, 6021.
[70] J. Xu, D. Su, W. Zhang, W. Bao, G. Wang, *J. Mater. Chem. A* **2016**, *4*, 17381.
[71] X. Chen, L. Yuan, Z. Hao, X. Liu, J. Xiang, Z. Zhang, Y. Huang, J. Xie, *ACS Appl. Mater. Interfaces* **2018**, *10*, 13406.
[72] M. Jagtoyen, F. Derbyshire, *Carbon* **1998**, *36*, 1085.
[73] C. Xu, Y. Wu, X. Zhao, X. Wang, G. Du, J. Zhang, J. Tu, *J. Power Sources* **2015**, *275*, 22.
[74] Q. Fan, W. Liu, Z. Weng, Y. Sun, H. Wang, *J. Am. Chem. Soc.* **2015**, *137*, 12946.
[75] X. Yuan, B. Liu, H. Hou, K. Zeinu, Y. He, X. Yang, W. Xue, X. He, L. Huang, X. Zhu, L. Wu, J. Hu, J. Yang, J. Xie, *RSC Adv.* **2017**, *7*, 22567.
[76] V. Marangon, E. Scaduti, V. F. Vinci, J. Hassoun, *ChemElectroChem* **2022**, *9*, e202200374.
[77] K. Yang, Q. Gao, Y. Tan, W. Tian, W. Qian, L. Zhu, C. Yang, *Chem. Eur. J.* **2016**, *22*, 3239.
[78] Y. Lai, P. Wang, J. Li, K. Zhang, Z. Zhang, *J. Electroanal. Chem.* **2017**, *805*, 120.
[79] Y. X. Yin, S. Xin, Y. G. Guo, L. J. Wan, *Angew. Chem. Int. Ed.* **2013**, *52*, 13186.
[80] F. Wu, Y. Ye, R. Chen, J. Qian, T. Zhao, L. Li, W. Li, *Nano Lett.* **2015**, *15*, 7431.
[81] A. Benítez, V. Marangon, C. Hernández-Rentero, Á. Caballero, J. Morales, J. Hassoun, *Mater. Chem. Phys.* **2020**, *255*, 123484.
[82] V. Marangon, J. Hassoun, *Energy Technol.* **2019**, *7*, 1900081.
[83] B. Boukamp, *Solid State Ionics* **1986**, *18–19*, 136.
[84] B. Boukamp, *Solid State Ionics* **1986**, *20*, 31.
[85] D. Di Lecce, T. Hu, J. Hassoun, *J. Alloys Compd.* **2017**, *693*, 730.
[86] W. Weppner, R. A. Hugguns, *J. Electrochem. Soc.* **1977**, *124*, 1569.
[87] D. Di Lecce, J. Hassoun, *J. Phys. Chem. C* **2015**, *119*, 20855.
[88] J. Molenda, W. Ojczyk, K. Swierczek, W. Zajac, F. Krok, J. Dygas, R. Liu, *Solid State Ionics* **2006**, *177*, 2617.
[89] K. Tang, X. Yu, J. Sun, H. Li, X. Huang, *Electrochim. Acta* **2011**, *56*, 4869.
[90] F. Luna-Lama, A. Caballero, J. Morales, *Sustain. Energy Fuels* **2022**, *6*, 1568.
[91] W. Wang, Y. Zhao, Y. Zhang, N. Liu, Z. Bakenov, *J. Mater. Sci. Technol.* **2021**, *74*, 69.
[92] M. A. Cabañero, N. Boaretto, M. Röder, J. Müller, J. Kallo, A. Latz, *J. Electrochem. Soc.* **2018**, *165*, A847.
[93] A. Benítez, J. Amaro-Gahete, Y.-C. Chien, Á. Caballero, J. Morales, D. Brandell, *Renewable Sustainable Energy Rev.* **2022**, *154*, 111783.
[94] Q. Cheng, Z.-X. Chen, X.-Y. Li, L.-P. Hou, C.-X. Bi, X.-Q. Zhang, J.-Q. Huang, B.-Q. Li, *J. Energy Chem.* **2023**, *76*, 181.
[95] X. Guo, K. Li, W. Bao, Y. Zhao, J. Xu, H. Liu, G. Wang, *Energy Technol.* **2018**, *6*, 251.

Manuscript received: November 9, 2022
Revised manuscript received: December 22, 2022
Accepted manuscript online: December 23, 2022
Version of record online: ■■, ■■■

RESEARCH ARTICLE

Choose carefully: The diffusion at the electrode/electrolyte interphase drives the performances of the lithium-sulfur battery, and determines the possible applicability of a cell using activated carbon with enhanced electrochemical conversion process in terms of relevant stability and fast kinetics.

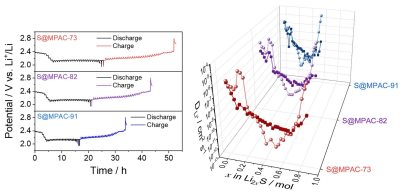

F. L. Lama, Dr. V. Marangon, Prof. Dr. Á. Caballero, Prof. Dr. J. Morales, Prof. Dr. J. Hassoun**

1 – 19

Diffusional Features of a Lithium-Sulfur Battery Exploiting Highly Microporous Activated Carbon